

1 **Calcite U-Pb dating of altered ancient oceanic crust in the North Pamir, Central Asia**

2 Johannes Rembe¹, Renjie Zhou², Edward R. Sobel¹, Jonas Kley³, Jie Chen⁴, Jian-xin Zhao², Yuxing Feng²,
3 Daryl L. Howard⁵

4 ¹ Institute of Geosciences, University of Potsdam, 14476 Potsdam-Golm, Germany

5 ² School of Earth and Environmental Sciences, The University of Queensland, St. Lucia QLD 4072,
6 Australia

7 ³ Department of Structural Geology and Geodynamics, Georg-August-Universität Göttingen, 37077
8 Göttingen, Germany

9 ⁴ State Key Lab. of Earthquake Dynamics, Xinjiang Pamir Intracontinental Subduction National Field
10 Observation and Research Station, Institute of Geology, China Earthquake Administration, X9GJ+RV
11 Chaoyang, Beijing, China

12 ⁵ The Australian Synchrotron, 800 Blackburn Rd Clayton, VIC 3168, Australia

13 Correspondence to: Johannes Rembe, jrembe@uni-potsdam.de and Renjie Zhou, renjie.zhou@uq.edu.au

14 **Abstract.** The North Pamir, part of the western syntax of the India-Asia collision zone, preserves remnants of a
15 poorly understood Paleozoic intra-oceanic subduction zone. To constrain the age of this ancient ocean floor, we
16 analyzed calcite phases in vesicular basalt and basaltic volcanic breccia with U-Pb geochronology using laser-
17 ablation inductively-coupled-plasma mass-spectrometry (LA-ICP-MS). Dating of radial-fibrous to equant spary
18 calcite yielded three meaningful Visian-Serpukhovian ages. REE + Y data reveal that the basaltic host rock of
19 the calcite and oxidizing seawater are major sources of trace elements during calcite precipitation. U-Pb ages
20 seem to be independent of REE + Y concentrations. Our results demonstrate the potential of calcite dating to
21 constrain the age of ancient ocean floors. We challenge the hypothesis that a continuous early Paleozoic Kunlun
22 Terrane extended from northern Tibet into the North Pamir.

23 **Summary.** Calcite is frequently formed during alteration processes in the basaltic, uppermost layer of juvenile
24 oceanic crust. Weathered oceanic basalts are hard to date with conventional radiometric methods. We show in a
25 case study from the North Pamir, Central Asia, that calcite U-Pb age data—supported by geochemistry and
26 petrological microscopy—has the potential to date sufficiently old oceanic basalts, if the time span between
27 basalt extrusion and latest calcite precipitation (~25 Ma) is considered.

28 **1 Introduction**

29 Constraining the timing of formation of ocean floor basalts is significant to develop models of various tectonic
30 processes given the voluminous occurrence of ocean floor basalts in ophiolites, sections of ocean plate
31 stratigraphy and exhumed subduction complexes, and remnants of island-arcs and oceanic plateaus in ancient
32 convergent margins. However, mafic volcanic rocks, in which zircons are sparse, are challenging to date with
33 radiometric methods. ⁴⁰Ar/³⁹Ar dating of separated phenocrysts or groundmass is frequently attempted (e.g.,
34 Waagstein et al., 2002; Heath et al., 2018). However, ocean floor alteration (OFA) often disturbs K-Ar isotopic
35 compositions by secondary potassium gain (Staudigel et al., 2013) or loss (Pringle, 2013), making ⁴⁰Ar/³⁹Ar

36 dating more successful in providing high precision age data for fresh volcanic rocks but problematic if samples
37 were affected by OFA.

38 Calcite veins and calcite-filled amygdules are commonly observed in submarine volcanic rocks. Studies show
39 that calcite formation occurs during OFA by alkalinity-generating reactions shortly after the eruption of lavas
40 (e.g. Coogan and Gillis, 2018; Spivack and Staudigel, 1994; Coogan et al., 2016), driven by the infiltrating
41 seawater and heat extraction from the oceanic crust. Such processes dominantly occur within ~25 Ma after rock
42 consolidation (Coogan and Gillis, 2018). Therefore, dating the calcite phases in ocean floor volcanic rocks has
43 the potential to constrain the timing of rock formation.

44 Calcite LA-ICP-MS U-Pb dating has been applied to a range of geological problems such as dating of
45 deformation (e.g., Nuriel et al., 2019), diagenesis, and sedimentation (e.g., Godeau et al., 2018), especially since
46 several international reference materials were established (Roberts et al., 2017; Rasbury et al., 2021). We present
47 calcite LA-ICP-MS U-Pb dating of Paleozoic oceanic crust from Central Asia. Several types of calcite were
48 dated from a volcanic sequence in the Carboniferous North Pamir arc (Figure 1, e.g., Bazhenov and Burtman
49 (1982)). Calcite U-Pb ages are consistent with regional geological data and existing radiometric ages from
50 correlative volcanic units. With additional petrographic and geochemical data, our work sheds light on the
51 potential of calcite U-Pb dating on ancient ocean floor volcanics and allows us to test tectonic models of the
52 Pamir.

53 **2 Geological background and motivation**

54 The North Pamir magmatic arc formed during subduction of the Paleo-Tethys oceanic lithosphere (e.g.,
55 Bazhenov and Burtman, 1982). The arc can be traced from the Chinese NE Pamir along strike into the Darvaz
56 mountain range in the Gorno-Badakhshan province of Tadjikistan and further south into the Badakhshan
57 province of Afghanistan (Figure 1). Outcrops in the Chinese Oyttag and Gez valleys have been correlated with
58 the South Kunlun Terrane in the north Tibetan West Kunlun by connecting ophiolitic sequences along the
59 proposed Oyttag–Kudi suture (e.g., Mattern et al., 1996). However, existing age dating reveals dissimilarities of
60 key rock units in this suture in the West Kunlun compared to the North Pamir. The West Kunlun Kudi suture
61 closed in the Silurian, as interpreted from zircon and monazite LA-ICP-MS U-Pb dating of amphibolite-facies
62 rock (Zhang et al., 2018). In contrast, the North Pamir magmatic arc, to which the mafic volcanic rocks and
63 associated plagiogranites in the Oyttag and Gez valleys are assigned, seems to be much younger. It consists of
64 poorly dated mafic and intermediate volcanics, associated volcanoclastic rocks, and subordinate cherts. A series
65 of leucogranites and granodiorites that intruded the arc between 360 and 314 Ma has been dated recently (Jiang
66 et al., 2008; Kang et al., 2015; Rembe et al., 2021; Zhang et al., 2006). The Oyttag suture itself is represented by
67 a small outcrop of altered ultramafic rocks in the Gez valley (Jiang, 1992). To date, no age data has been
68 presented for those rocks. The green color of the North Pamir arc volcanic rocks implies thorough spilitization,
69 making them unsuitable for $^{40}\text{Ar}/^{39}\text{Ar}$ dating. We propose that abundant calcite associated with spilitic basalts are
70 a product of OFA, and that calcite ages can serve as a constraint on the formation of ocean floor. Specifically,
71 they provide the possibility of directly dating OFA as a proxy for the emplacement age of mafic volcanic rocks.

72 We conducted calcite dating based on detailed petrographic and geochemical observations in order to provide
73 age constraints on the North Pamir arc volcanic rocks and test its correlation with the West Kunlun. For that

purpose, we sampled 4 specimens at 3 different localities in the Chinese Qimqan valley (Figure 1). Samples 17NP436a and 17NP436b are from the same locality (sample location at N 39° 18' 27", E 74° 51' 32") and represent redeposited brecciated mafic volcanic rock with interstitial calcite cement that was formed during an early phase of brecciation (Figure 2a–c). Samples 15NP236 (sample location at N 39° 18' 18", E 74° 51' 30") and 15NP233 (sample location at N 39° 18' 16", E 74° 51' 47") are from two localities with amygdaloid-basalt, where 15NP236 was taken from a pillow basalt. We investigated amygdules filled exclusively with calcite (Figure 2e, f)

3 Methods

3.1 Petrological microscopy, cathodoluminescence microscopy (CL) and X-ray fluorescence microscopy (XFM)

Petrographic thin sections of all samples were studied with conventional light microscopy and cathodoluminescence microscopy (CL). Polished thin sections of all samples were prepared. CL imaging was done using an Olympus BXFM-F microscope equipped with a Lumic hot-cathode electron source and a highly sensitive Olympus XC10 camera at the University of Potsdam. We recognized well preserved primary features (see Sect. 4.1), which were then identified on the rock chips prepared for laser ablation. Detailed sample petrography raises the chances of obtaining robust, meaningful ages, as emphasized recently by Roberts et al. (2021). High resolution reflected light images indicate the position of ablation spots in Appendix A.

Additionally, we examined sample 17NP436a with scanning X-ray fluorescence microscopy (XFM). A polished slab cut parallel to the surface examined with LA-ICP-MS was prepared from the same rock chip. XFM maps were collected at the XFM beamline at the Australian Synchrotron (Howard et al., 2020). The incident excitation energy was 18.5 keV. Pixel size and dwell time per pixel are indicated in the figures in Appendix B.

3.2 Laser-ablation inductively-coupled-plasma mass-spectrometry (LA-ICP-MS)

Rock samples were processed at the School of Earth and Environmental Sciences, The University of Queensland. Samples 15NP233 and 15NP236 were cut and mounted on one-inch diameter round mounts (Figure 2e, f); for samples 17NP436a and 17NP436b, we used polished rock chips (Figure 2b, c). Sample mounts were polished using standard polishing procedures and finished with a 0.25 micrometer diamond suspension.

LA-ICP-MS U-Pb dating and geochemical analysis was performed at the Radiogenic Isotope Facility of the Centre for Geoanalytical Mass Spectrometry, The University of Queensland following methods in Su et al. (2020) and Yang et al. (2021). Laser ablation was achieved using an ASI RESOLUTION 193 ArF nm excimer laser system. Following evacuation of air, He carrier gas was introduced into the laser cell at a flow rate of 0.35 l/min. 0.005 l/min of N₂ gas was also introduced to the laser cell to enhance the measurement sensitivity. The gas mixture was then introduced into the plasma torch of a Thermo iCAP RQ quadrupole ICP-MS with 1.06 l/min Ar nebulizer gas. No reaction gas was employed. The laser was run with a 100 µm diameter round spot at 10 Hz, with a measured instrument laser-fluence (laser pulse energy per unit area) of 2.5 J/cm². For U-Pb dating, each spot had 8 s of background, 20 s of data acquisition, and 15 s of wash out. For trace elemental analysis, each spot had 6 s of background, 25 s of data acquisition, and 10 s of wash out. Prior to data acquisition, ICP-MS signals

were optimized during tuning. For our session, ~950 kcps of ^{238}U counts and ~0.22 of $^{206}\text{Pb}/^{238}\text{U}$ were achieved for measuring NIST612 glass using line scans of 3 $\mu\text{m/s}$, 10 Hz, 50 μm round laser pit, and 3 J/cm^2 .

U-Pb isotopes for geochronology (^{206}Pb , ^{207}Pb , ^{208}Pb , ^{232}Th , and ^{238}U) were measured with the following dwell times, ^{206}Pb (0.025 s), ^{207}Pb (0.055 s), ^{208}Pb (0.005 s), ^{232}Th (0.005 s), and ^{238}U (0.02 s). Both glass standard NIST614 and matrix-matched calcite standards were measured, bracketing unknown spots. NIST614 glass was used for correction of $^{207}\text{Pb}/^{206}\text{Pb}$ fractionation and instrument drift in the $^{238}\text{U}/^{206}\text{Pb}$ ratio (Woodhead and Hergt, 2001). Raw data were processed using Iolite software v3.64 (Paton et al., 2011). After the initial correction, a matrix-matched calcite reference material of known age was used for further correction of matrix-related mass bias impacting the measured $^{238}\text{U}/^{206}\text{Pb}$ ratios, following the approach described elsewhere, as summarized in Yang et al. (2021). We used cross-calibrated in-house calcite reference materials AHX-1D and PTKD-2 and an international reference material WC-1 (Roberts et al., 2017) in our laser ablation session. The accuracy of unknown spots is checked by measuring WC-1 and PTKD-2 as monitoring standards. For WC-1 we obtained an age of 251 ± 1 Ma (2σ), consistent with the recommended age of 254.4 ± 6.4 Ma (Roberts et al., 2017). The in-house PTKD-2 standard gave an age of 154 ± 3 (2σ), consistent with our recommended age of 153.7 ± 1.7 Ma (2σ), calibrated by isotope dilution. Therefore, we note that the accuracy for our measurements can be calculated as 1.5 % for WC-1 and 0.3 % for PTKD-2. Uncertainty propagation was done according to the principles defined by Horstwood et al. (2016). We present two age uncertainties as $\pm\alpha/\beta$ (2σ), where α is without propagated systematic uncertainties, and β is with propagated systematic uncertainties. We propagated our analytical errors (typically <5% (2σ) on $^{238}\text{U}/^{206}\text{Pb}$ ratios) by incorporating ^{238}U decay constant error, long-term variance of the reference materials $^{238}\text{U}/^{206}\text{Pb}$ ratios in the lab, and the analytical error of the monitor standard. This resulted in a total propagated systematic uncertainty of 4.6% (2σ) into the analytical error.

Trace elemental analysis was conducted in the same ablation areas as the U-Pb spots but without overlapping the U-Pb spots. Prior to data acquisition, ICP-MS signals were optimized during tuning while the oxide production rate was controlled to be as low as possible. The ThO/Th ratio during our session was <0.002 for NIST612 glass using line scans of 3 $\mu\text{m/s}$, 10 Hz, 50 μm round laser pit, and 3 J/cm^2 . ^{43}Ca was measured as an internal standard. Data reduction was conducted using the Iolite software v3.64 (Paton et al., 2011) with the Trace Element data reduction scheme. All reported concentrations were after international standardization using Ca ($\text{Ca} = 40.1$ %).

4 Results

4.1 Petrography and calcite occurrences

In the Chinese Qimgan valley, basaltic to andesitic volcanic rocks contain large amounts of calcite in amygdules, in between single lava pillows, and volcanic breccia layers (Figure 2 and Appendix A). Two samples, 15NP233 and 15NP236, are altered amygdaloid-basalts with published geochemistry (Supplementary Table 1, Rembe et al., 2021). Samples 17NP436a and 17NP436b are from a volcanic breccia, rich in calcite cement fragments and calcite-overgrown, angular volcanic rock fragments. The samples were collected from 3 localities, whereas 17NP436a and 17NP436b are from the same locality.

Amygdules in samples 15NP233 and -236 show one generation of spary or botryoidal calcite with typical sweeping extinction under cross-polarized light (Figure 3a, b). Sample 15NP233 has vesicles up to 5 mm in

diameter filled exclusively with calcite. Sample 15NP236 has much smaller vesicles, around 1 mm in diameter, filled with either calcite or zeolite. Both samples show high “Loss on Ignition” (LOI) values and anomalous major element values for whole rock geochemistry, accounting for high secondary, volatile rich mineral content (Supplementary Table 1). No fractures or veins cut across amygdules in these samples.

In samples 17NP436a and b, fracture and pore space in basaltic rock fragments shows multiple calcite generations (Figure 3c, d). Most calcite formed prior to deposition of the breccia. Specifically, isolated cement fragments are fully embedded in a fine-grained matrix (e.g., in sample 17NP436b). They may have formed in fractures of a volcanic edifice and were redeposited after its collapse. In some cases, calcite cement is still attached to the basaltic clasts and a series of 4 consecutive mineralization phases can be recognized (numbered 1 to 4 in Figure 3d, schematically depicted in Figure 3e-g). Some of the volcanic rock fragments show an early, hydrothermal clay layer (Figure 3c and phase 1 in Figure 3d). The rock fragments—or if present, the clay coatings—are overgrown by a first generation of radial-fibrous calcite. Larger voids are filled with late, equant calcite (phase 2 and 3 in Figure 3d). The early, medium to coarse spary calcite cements (2 and 3 in Figure 3d) and the matrix are crosscut by fine-sparitic calcite filled fissures (4 in Figure 3d). The fissures are distinguishable from the spary calcite in transmitted and reflected light and were avoided during ablation.

Cathodoluminescence microscopy imaging reveals fibrous botryoidal textures of the vesicle-filling calcite of samples 15NP233 and 15NP236. They usually show no luminescence or a zonation of dull-yellowish and non-luminescent fringes (Figure 4a,b). Bright yellow luminescence irregularly occurs along the rims of the vesicles. Secondary fractures crosscutting the vesicular fabric were not observed. We prepared slides from the rock chips analyzed with LA-ICP-MS of samples 17NP436a and 17NP436b (Figure 4c-f). The basalt breccia samples 17NP436a and 17NP436b show non-luminescent to dull yellow luminescent spary calcite. Bright yellow luminescence was observed along hairline subzones, which are interpreted as grain boundaries. The largely non-luminescent spary calcite fragments stand out against the yellow luminescent altered volcanoclastic matrix. Matrix and spary calcite fragments are intersected by bright-yellow, late-stage calcite (phase 4 in Figure 3d) filled fractures (e.g., Figure 4c). They are clearly visible in transmitted and reflected light and were avoided during ablation.

In order to better understand calcite phases, we further study 17NP436a with high-resolution synchrotron X-ray fluorescence mapping (Howard et al., 2020), following methods described in Vanghi et al. (2019). Sr maps show elevated concentration for the phase 2 and 3 calcite and much lower content in fissure filling calcite phase 4, suggesting different geochemical regimes (Appendix B).

4.2 LA-ICP-MS U-Pb Dating

Four samples from three field sites were prepared for analysis. We obtained data from 839 single spots from 18 laser ablation areas (Appendix A), 3–6 ablation areas per sample (Figure 5, Figure 6), data table in Supplementary Table 2. For age calculation, we used the IsoplotR program (Vermeesch, 2018) version 3.5 running in R version 3.6.0. Ages are calculated for individual ablation areas by linear regression in a Tera–Wasserburg plot. From the 839 single spot ablation data only 16 had to be omitted due to U content below the detection limit.

4.2.1 17NP436a

Six ablation areas were targeted in basalt breccia sample 17NP436a (Figure 5a-f). They are placed on isolated coarse sparitic, equant calcite cement fragments (areas A, C, D, E) and coarse-sparitic radial-fibrous to equant calcite cement still connected to their basaltic substratum (areas B, F). Propagated errors are generally small (~5%) and MSWD values are low to moderate. Area A is an isolated fragment of coarse spary cement (Figure 4c) and yielded a lower intercept age of $331 \pm 2/15$ Ma (MSWD = 1.7) calculated from 119 single spot data points. Eighty-two ablation spots yielded a lower intercept age of $324 \pm 4/16$ Ma (MSWD = 2.3) for Area B. Sixty-four ablation spots gave a lower intercept age of $308 \pm 7/16$ Ma (MSWD = 2.5) for Area C. Area D gave a similar lower intercept age of $307 \pm 6/15$ Ma (MSWD = 4.2, n = 40). Area E gave a rather low age of $298 \pm 10/17$ Ma with an elevated MSWD of 4.7, defined by 37 ablation spots. Sixty-one ablation spots on area F (Figure 4f) defined a lower intercept age of $304 \pm 7/16$ Ma (MSWD = 3.5).

4.2.2 17NP436b

In basalt breccia sample 17NP436b, four ablation areas were targeted (Figure 5g-j). They are placed on isolated coarse sparitic, equant calcite cement fragments. Propagated errors are generally small (~5%) and MSWD values are low to moderate. Area A (Figure 4d) yielded a lower intercept age of $339 \pm 6/17$ Ma (MSWD = 1) defined by 38 ablation spots. Area B yielded a lower intercept age of $322 \pm 3/15$ Ma (MSWD = 4.8) defined by 47 ablation spots. Twenty-nine laser spots on area C (Figure 4e) yielded a lower intercept age of $328 \pm 4/16$ Ma (MSWD = 1.7). Twenty-three ablation spots gave a lower intercept age of $316 \pm 9/17$ Ma (MSWD = 2.4).

4.2.3 15NP236

Five ablation areas were targeted in vesicular basalt sample 15NP236 (Figure 6a-e). Each ablation area represents one calcite filled vesicle. Due to the small vesicles, only a few spots were placed per area. Propagated errors are moderate to large (6-36%) and MSWD values are low to moderate. Area A yielded a lower intercept age of $351 \pm 29/33$ Ma (MSWD = 2.2) defined by 14 single ablation spots. Fifteen ablation spots on area B gave a lower intercept age of $306 \pm 64/65$ Ma with a low MSWD of 1.4. Ten spots on area C gave an age of $350 \pm 15/22$ Ma (MSWD = 2.2). Area D yielded a very young age of $206 \pm 73/73$ Ma (MSWD = 0.84) defined by 10 ablation spots. A similarly young age of $272 \pm 57/58$ Ma (MSWD = 4.3) was defined by 18 laser spots for area E.

4.2.4 15NP233

Three ablation areas were placed on calcite in three filled vesicles in sample 15NP233 (Figure 6f-h). Propagated errors are small (~5%) and MSWD values are moderate. Area A gave an age of $324 \pm 4/16$ Ma (MSWD = 2.4) defined by 60 ablation spots. Ninety-nine ablation spots on area B yielded a similar age of $327 \pm 5/16$ Ma (MSWD = 2.5). Fifty-eight ablation spots on area C gave a slightly higher age of $337 \pm 7/17$ Ma (MSWD = 9.8).

4.3 LA-ICP-MS Geochemistry

For each laser ablation area, we measured Ca, Mn, Sr, Zr, Ba and REE + Y geochemical data (a total of 380 single spot analyses) using LA-ICP-MS (data in Supplementary Table 3). Calcite REE patterns normalized to chondrite (Boynton, 1984) are mostly flat to slightly “U” shaped (Appendix C). REE content of the vesicle-hosted calcite is higher (61 ppm mean total REE content in sample 15NP233, 59 ppm in sample 15NP236)

compared to the breccia calcite cement (8 ppm in 17NP436a and 12 ppm in 17NP436b). LREE are enriched over MREE (La_n/Sm_n) and negatively correlate with enriched MREE over HREE values (Dy_n/Yb_n) in all samples. The vesicle-filling calcite shows both positive and negative Ce/Ce^* values between 0.75 and 1.4; the breccia calcite cement shows negative values between 0.18 and 0.92. Negative Ce anomalies are usually associated with oxidizing conditions producing Ce^{4+} instead of Ce^{3+} (e.g., Alibo and Nozaki, 1999). We observe positive to slightly negative Gd anomalies ($\text{Gd}/\text{Gd}^* = \text{Gd}_n/\sqrt{\text{Eu}_n \times \text{Tb}_n}$; Figure 7a). Positive Y_n/Ho_n anomalies are common (Figure 7b). Negative Ce/Ce^* and Eu/Eu^* anomalies together with higher Gd/Gd^* and Y_n/Ho_n in the calcite cement of the volcanic breccia are interpreted to reflect a stronger influence of infiltrating seawater ($\text{Ce}/\text{Ce}^* = \text{Ce}_n/\sqrt{\text{La}_n \times \text{Pr}_n}$; $\text{Eu}/\text{Eu}^* = \text{Eu}_n/\sqrt{\text{Sm}_n \times \text{Tb}_n}$).

5 Discussion

5.1 Calcite age data and its significance

In newly formed submarine volcanic rocks, calcite formation marks the phase of alkalinity-generating reactions. Alkalinity describes the acid neutralizing capacity by formation of alkali and alkaline earth metal ion species during rock weathering (e.g., Spivack and Staudigel, 1994). This is crucial for interpreting OFA calcite U-Pb ages, implying that these ages should be no older than the “true” rock formation age. High temperature hydrothermal alteration is also a common phenomenon in submarine volcanic environments. This is, in contrast, restricted to discrete zones, such as veins, shear zones, and hydrothermal upflow zones (Harlov and Austrheim, 2013; Honnorez, 2003). It changes the mineral composition of the volcanic host rock completely, such that primary igneous textures are obliterated (e.g. epidiosites, Honnorez, 2003). Such rock types must be avoided as they are unlikely to produce ages related to OFA. By dating isolated calcite, far from hydrothermal upflow zones, we determine the age range of OFA that occurred shortly after rock consolidation. This gives a minimum age estimate for ocean floor formation, if not the actual age of formation. This must not be mistaken for the radiometric ages of the volcanic rock itself (e.g., ages from zircon U-Pb dating).

We observed one botryoidal to spary calcite phase in the vesicular basalts (Figure 3a, Figure 4a, b). Four stages of mineralization were observed in the basaltic breccia: (1) hydrothermal clay, (2) radial-fibrous calcite, (3) coarse equant-spary calcite and (4) fissure filling calcite crosscutting the entire fabric (Figure 3b-g). The presence of radial-fibrous and sparry, equant calcite crystals is typical of continuous calcite precipitation in a porous substratum (Gonzalez and Carpenle, 1992). In a first phase, radial-fibrous calcite grows along the wall of the voids and successively reduces the porosity of the substratum, thereby hindering fluid flow. This reduces the calcite precipitation rate and the amount of nucleation, leading to larger, equant calcite crystals in the center of the voids. This model can be adopted for a first calcite phase (2 and 3 in Figure 3d). As the radial-fibrous and the equant calcite growth reflects one process, both calcite phases were chosen for ablation. The phase 4 fine-sparitic filled fissures are interpreted to reflect a later tectonic event, expressed by differential stress, pressure solution and reprecipitation of calcite in open joints (Figure 3g).

To explore the geologic significance of our age data, we first applied a very conservative filter, closely examining ages with $\text{MSWD} < 2$ and $2\sigma\text{-error} < 10\%$, as their isotope ratios are most likely measured from

single homogenous domains (e.g., Lan et al. (2022)). Subsequently, we also discuss all ages for a full view of the age spectrum.

Our samples generally show a low variability in ablation area ages and initial Pb values (Figure 5 and Figure 6). 2σ -errors with propagated systematic uncertainties are typically around 5%; only vesicular basalt sample 15NP236 shows high 2σ -errors. However, multi-stage calcite formation and possible subsequent alteration lead to MSWD values above two and elevated age errors. Primary calcite was eventually affected by alteration and crystallization of calcite with differing chemistry even within microscopically identified seemingly homogenous phases (e.g. phase 2 and 3 in Figure 3d). This is made visible by CL imaging of yellow-luminescent subzones penetrating non-luminescent phase 2 and 3 calcite zones in Figure 4f. However, ablation spots placed on ablation areas 17NP436a_A, 17NP436b_A and 17NP436b_C largely fall on what we interpret as phase 2 and 3, radial-fibrous to equant calcite, characterized by non-luminescence (Figure 4c-e). The lower intercept ages are $331 \pm 2/15$ Ma (17NP436a_A), $339 \pm 6/17$ Ma (17NP436b_A) and $328 \pm 4/16$ Ma (17NP436b_C), which consistently constraints the volcanic breccia to the Visean-Serpukhovian boundary. All ablation areas of basalt breccia samples 17NP436a and 17NP436b and vesicular basalt sample 15NP233 overlap within propagated 2σ -errors. Their scatter reflects either the mixed ages of multiple calcite formation events during the late Mississippian to Pennsylvanian which cannot be resolved, or minor isotope disturbance (by heating and/or fluid flow) during a much younger event. Vesicular basalt sample 15NP236 yielded less defined regressions, thus high age errors, caused by the small spread of the limited number of ablation spots. However, two ablation areas, 15NP236_B and 15NP236_D, gave MSWD values of 1.4 and 0.84 respectively, while yielding much different lower intercept ages. 15NP236_B gave an age of $306 \pm 64/65$ Ma, which overlaps with the ages of 15NP236_A ($351 \pm 29/33$ Ma, MSWD = 2.2) and 15NP236_C ($350 \pm 15/22$ Ma, MSWD = 2.2). 15NP236_D gave an age of $206 \pm 73/73$ Ma, which is apparently younger. This leads us to conclude that Carboniferous primary ages were affected by young events causing isotope disturbance and shift of the apparent, yet mixed ages towards younger values. This might be true to a limited degree for all samples with MSWD > 2.

Calcite ages are consistent with published radiometric ages of correlative rock units in the North Pamir arc, including two hornblende $^{40}\text{Ar}/^{39}\text{Ar}$ ages of ~350 Ma from a meta-andesite, zircon U-Pb ages of ~329 Ma from felsic to intermediate volcanics in Altyn Darya valley (Schwab *et al.*, 2004), and zircon U-Pb ages of ~360 to 314 Ma from island arc granites (Ji et al., 2018; Rembe et al., 2021) (Figure 8). All these ages are interpreted by the aforementioned authors to be primary magmatic ages and reflect the age of emplacement of those units.

5.2 Calcite REE + Y geochemistry

Whole rock geochemical data from altered basalt has a flat C1-normalized REE pattern (Boynnton, 1984), implying an intra-oceanic arc origin (Jiang et al., 2008; Rembe et al., 2021). We suggest a possible control of the basalt geochemistry on calcite REE patterns; any process altering this signal would significantly change the calcite REE pattern (Debruyne et al., 2016).

REE partition coefficients between aqueous solution and precipitating calcite have been experimentally studied (e.g., Perry and Gysi, 2018; Voigt et al., 2017); results suggest that variable physicochemical conditions could lead to strongly differing integration of rare earth elements into the calcite lattice. We show that calcite cements

of samples 17NP436a and b are distinguishable from vesicle fillings in samples 15NP233 and -236 (Figure 7a, b).

Calcite must be the major REE + Y sink as our samples do not show any intergrowing, co-precipitated mineral phase. The dominance of calcite hints at precipitation from CO₂-rich seawater derived hydrothermal fluids under low temperature conditions (Talbi and Honnorez, 2003; Honnorez, 2003). This happened in the upper few 100 meters of the oceanic crust. We assume a low mineralization temperature. Under this condition, Eu is trivalent and negative Eu/Eu* is directly inherited from the fluid reservoir (Debruyne et al., 2016). Pronounced negative Ce/Ce* values are a typical inherited signal of oxidizing seawater (e.g., Alibo and Nozaki, 1999); in correlation with increasing Y_n/Ho_n values, they trace back to oxidative sorption by Fe-Mn O(OH) species (Debruyne et al., 2016). Positive Gd/Gd* values may be interpreted as a seawater signal (e.g., Baar et al., 1985). However, markedly positive Gd anomalies together with positive Y_n/Ho_n values are less commonly reported. Similar features were observed in high salinity waters from Jordan graben lakes (e.g., Möller et al., 2007). Because ocean floor aquifer porosities are highly heterogeneous (e.g., Fisher and Becker, 2000), the higher porosity of volcanic breccias 17NP436a and 17NP436b may have promoted seawater infiltration, leading to lower REE concentrations and more pronounced Ce/Ce*, Eu/Eu*, Gd/Gd* and Y_n/Ho_n anomalies compared to amygdaloidal basalt samples. We note that Gd anomalies strongly correlate with REE concentration. Although, LA-ICP-MS data acquisition was done according to international standards, we cannot completely exclude the possibility of polyatomic interference of the measured ¹⁵⁷Gd isotope with ¹⁴¹Pr¹⁶O⁺ (May and Wiedmeyer, 1998).

5.3 Implications on tectonic models of the Pamir

The results from petrological thin section examination, showing primary calcite fabrics, together with LA-ICP-MS trace element geochemistry, which reflect sea water infiltration, typical for OFA, are major arguments for preserved, primary U-Pb isotopic ratios. Our studies constrain the emplacement age of arc volcanic rocks in the NE Pamir to Middle-Upper Mississippian (Visean-Serpukhovian) (Figure 8), significantly younger than correlative lithologies in the West Kunlun, which are dated to the Cambrian (e.g. Yixieke dacite, Xiao et al. (2005), Kudi ophiolite, Wang et al. (2021)). The results carry significant implications for the interpretation of the Mesozoic and Cenozoic geodynamic evolution of the Tibet-Pamir orogen. Since the pioneering works of Burtman et al. (1963), Burtman and Molnar (1993), Pan (1994), Mattern et al. (1996), Xiao et al. (2002) and references therein, the Kudi-Oytag suture, or the “Paleozoic suture”, has been hypothesized to be a single, once continuous, E–W-striking feature that was bent towards the north by Cenozoic indentation of the Pamir into a postulated Tarim-Tajik block.

Recent publications outline an early Paleozoic history of the West Kunlun arc magmatism (Figure 9a). The southward subduction of the Proto-Tethys started in the Terreneuvian, dated by the 531 Ma Nanpingxueshan pluton in the Tianshuihai Group (Yin et al., 2020). As a consequence of the development of the Yixieke volcanic arc (Xiao et al., 2005) and the Yierba arc, the South Kunlun was intruded by the Yierba adakitic diorite at ca. 513 Ma (Yin et al., 2020). In response to slab roll-back, the Kudi ophiolite formed in a back-arc position between 513–516 Ma (Wang et al., 2021). The Proto-Tethys closed in the Silurian between 431–420 Ma (Wang et al., 2020) with exhumation of metamorphic units starting from ca. 440 Ma, as dated by monazite U-Pb from the Saitula Group (Zhang et al., 2018). Closure of the Proto-Tethys was followed by the intrusion of A-type post-

orogenic granites, dated as 420–405 Ma by zircon U-Pb in the North Kudi granite (Yuan et al., 2002; Liu et al., 2014).

However, corresponding early Paleozoic geologic events or rock records in the North Pamir have not been reported. Instead, previous works on mafic to intermediate volcanic rocks and granitoids of the North Pamir show major subduction related arc magmatic activity in the mid to late Carboniferous (Rembe et al., 2021; Jiang et al., 2008; Ji et al., 2018; Kang et al., 2015; Ruzhentsev et al., 1977). Carboniferous arc magmatic rocks found in the Waqia (Tang et al., 2020) and East Mazar (Li et al., 2006) tectonic slivers reflect the closure of a remnant ocean basin, whereas major arc magmatic activity was focused on the North Pamir arc further to the west (Figure 9b). Stratigraphic relations and hiatus point to a soft collision and obduction of that North Pamir arc in the early Permian (Rembe et al., 2021). No broad Paleozoic magmatic activity younger than Lower Devonian is known in the West Kunlun. The Carboniferous North Pamir arc granitoids intrude largely into poorly dated mafic volcanic rocks. Our calcite U-Pb ages agree with the only known ages of this volcanic unit from Schwab et al. (2004) (Figure 8). They corroborate the dissimilarity of the West Kunlun and North Pamir arc volcanic rocks, and therefore argue against the existence of a continuous Paleozoic suture extending from the Pamir to the West Kunlun.

Recent studies on the Gissar and Kyzylkum segment of the South Tien Shan (STS) of Uzbekistan (Figure 1), west of the North Pamir, document the presence of early Carboniferous metamorphism and constrain the volcanic age of meta-basalts from the northern Kyzylkum segment by zircon U-Pb dating to 320–300 Ma (Konopelko et al., 2019 and references therein). This is coeval with arc magmatic activity along the North Pamir arc. Konopelko et al. (2019) propose an archipelago model for the late Paleozoic suture zones in the STS, characterized by high-T metamorphism, rapid exhumation, and multiple subduction zones. This archipelago might have been connected to the Paleo-Tethys realm. We argue for a North Pamir arc continuing from the northeastern Pamir into the Tajik northwestern Pamir and the Gissar segment of the South Tien Shan.

6 Conclusion

Calcite phases in Paleozoic ocean floor volcanic rocks were studied with LA-ICP-MS. From four samples, we investigated a total of 18 laser ablation areas. Although systematic errors of lower intercept ages could be small (as low as $<1\%$ at 2σ), we focus on propagated errors because they include the long-term variance of the reference materials, the analytical error of the monitor standard, and other important sources of errors. Three ablation areas yielded high quality lower intercept ages, 331 ± 15 Ma (17NP436a_A), 339 ± 17 Ma (17NP436b_A) and 328 ± 16 Ma (17NP436b_C), each with MSWD < 2 and propagated 2σ -error $< 10\%$, which we interpret as representing the timing of individual geologic events. The majority of the remaining ablation area ages from volcanic breccia samples 17NP436a and 17NP436b as well as vesicular basalt sample 15NP233 overlap with this age within propagated 2σ -errors. They show slightly elevated MSWDs, implying that they are mixed ages. Sample 15NP236 has the most complex age results, possibly caused by more severe disturbance of the isotope ratios by younger events. Ages of samples 17NP436a, 17NP436b and 15NP233 agree with existing radiometric ages of correlative volcanic units in the North Pamir, demonstrating that calcite formed during ocean floor volcanism, due to coeval or subsequent ocean floor alteration, provides a valuable age constraint on the

timing of volcanism. We note that these calcite ages do not directly date the formation of these volcanic rock but provide minimum age constraints within a timespan of about 25 Ma of ocean floor alteration.

Age data must be evaluated in the light of detailed petrographic analysis, including petrographic microscopy and cathodoluminescence microscopy, as well as geochemistry of the investigated calcite. Geochemical data supports our hypothesis of an ocean floor alteration-related origin of the investigated calcite. However, we underline that interpretation of REE content in calcite is not straight forward, since the trace element uptake by calcite is dependent on a multitude of factors.

The presence of Middle to Upper Mississippian ocean floor in the North Pamir argues against models invoking a continuous, early Paleozoic Kunlun belt, stretching from the West Kunlun far into the North Pamir. Instead, they support the presence of a mid to late Carboniferous volcanic arc system, tying the North Pamir more to comparative units in the Tien Shan.

7 Appendices

Appendix A: Reflected light images, Fig.A1–A4

Appendix B: X-ray fluorescence microscopy (XFM) maps, Fig. B1–6

Appendix C: REE data of each ablation area, Fig.C1

8 Code and data availability

Whole rock geochemistry data used from literature (Rembe et al. (2021), S1) as well as LA-ICP-MS isotope data (S2) and geochemistry (S3) will be uploaded to UQ eSpace (<https://espace.library.uq.edu.au/>), run by the University of Queensland.

9 Author contribution

JR, RZ, ERS, and JK conceptualized the project. Fieldwork was carried out by JR, ERS, JK, and CJ. Methodological concept preparation, laboratory work and data interpretation was done by RZ, JR, JXZ, YF, and DLH. JR prepared a first draft of the manuscript and all authors contributed to the review and editing procedure.

10 Competing interests

All authors declare that they do not have any conflict of interest.

11 Acknowledgement

We thank Langtao Liu for help with field work, and Antje Musiol and Baiansuluu Terbishalieva for support with laboratory work at the University of Potsdam. We are thankful for suggestions and constructive comments of

397 Dimitry Konopelko, Alexander Robinson and an anonymous reviewer. We also thank the editor Daniela Rubatto
398 for the assistance and the handling of the manuscript.

399 **12 Funding statement**

400 The project was funded by Deutsche Forschungs Gesellschaft e.V. (DFG) grant SO 436/12-1 to Sobel and DFG
401 grant KL 495/27-1 to Kley. Additional support was provided by grants to Sobel, Zhao and Zhou through the
402 Australia-Germany Joint Research Cooperation Scheme, to Howard and Zhou through the Australian
403 Synchrotron Access Program and to Zhou through a UQ ECR grant. Chen was supported by grants through the
404 2nd Tibetan Plateau Scientific Expedition and Research Program (STEP, 2019QZKK0901) and State Key Lab. of
405 Earthquake Dynamics of China (LED2016A05).

406

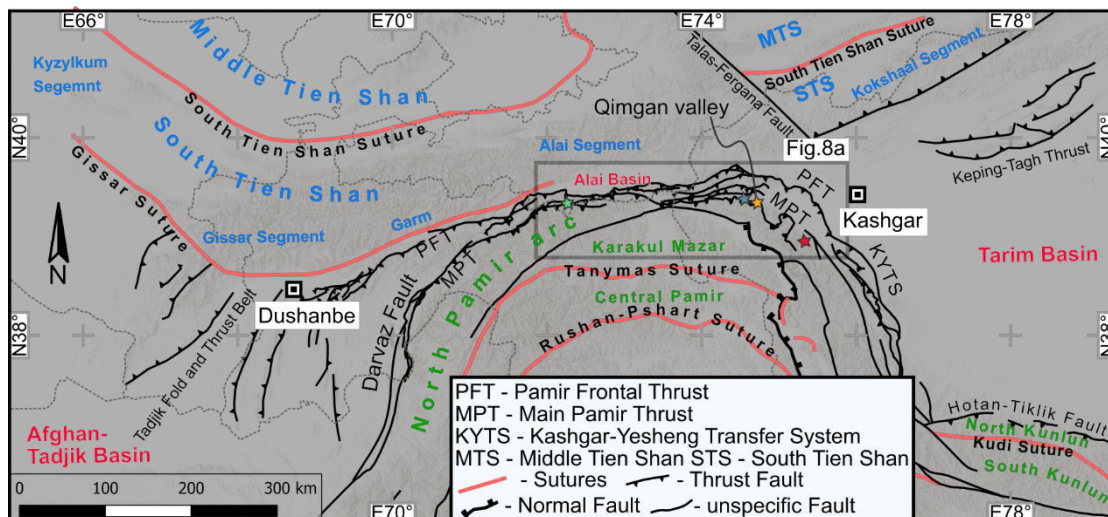


Figure 1: Overview map of the North Pamir and surroundings. The yellow star marks the position of the Qimqan valley, as noted. The meaning of the other star symbols are explained in Figure 8. Map drawn after Konopelko et al. (2019), Li et al. (2020), and Henan Institute of Geological Survey (2014).

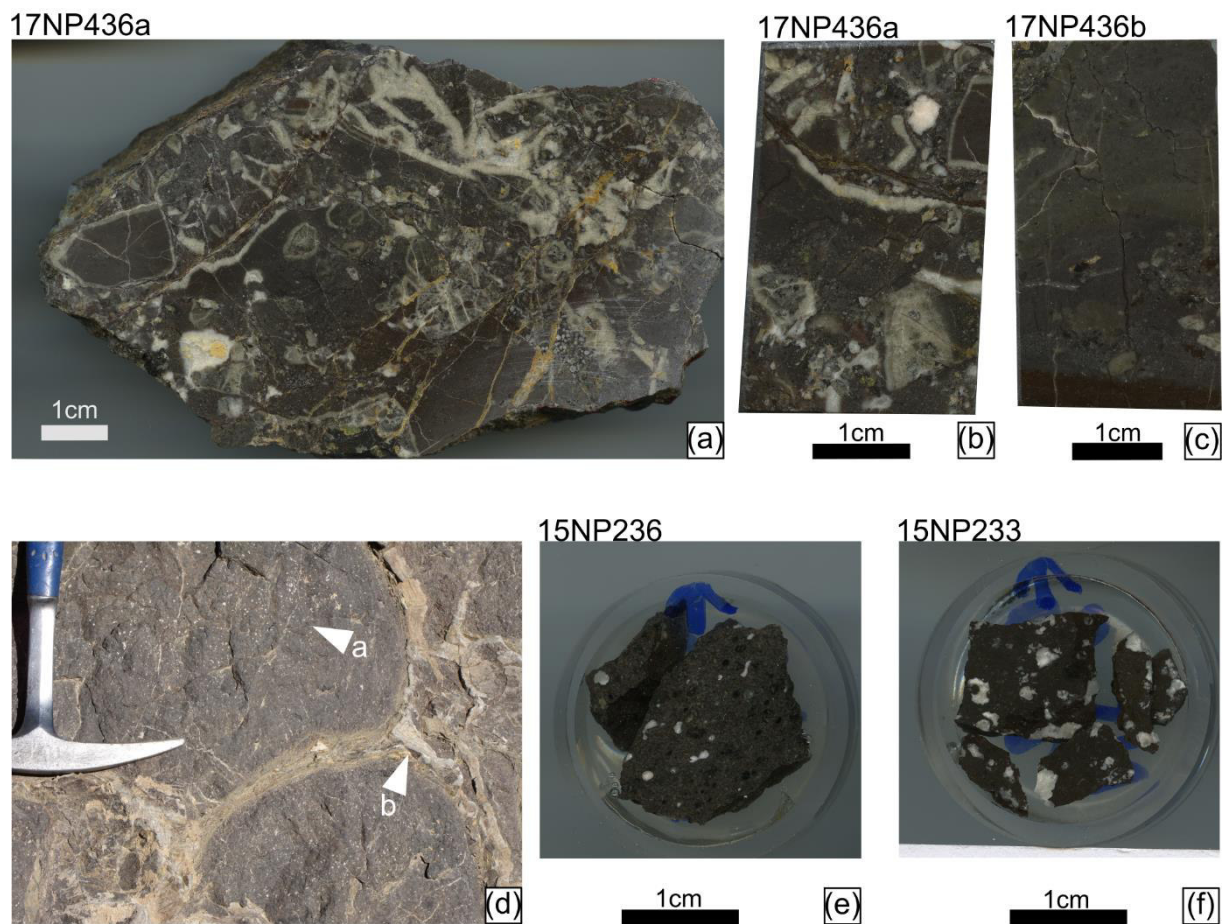


Figure 2: Photographs of hand specimen of sample 17NP436a (a) and polished rock block used for LA-ICP-MS measurements of sample 17NP436a (b) and 17NP436b (c). Field photograph of well-preserved amygdaloidal pillow-basalts in Oytay valley near Qimgan valley (d), with white arrows pointing at calcite filled vesicles (arrow a) and massive interstitial calcite (arrow b). Polished rock specimen 15NP236 (e) and 15NP233 (f) of similar rock, were used for LA-ICP-MS.

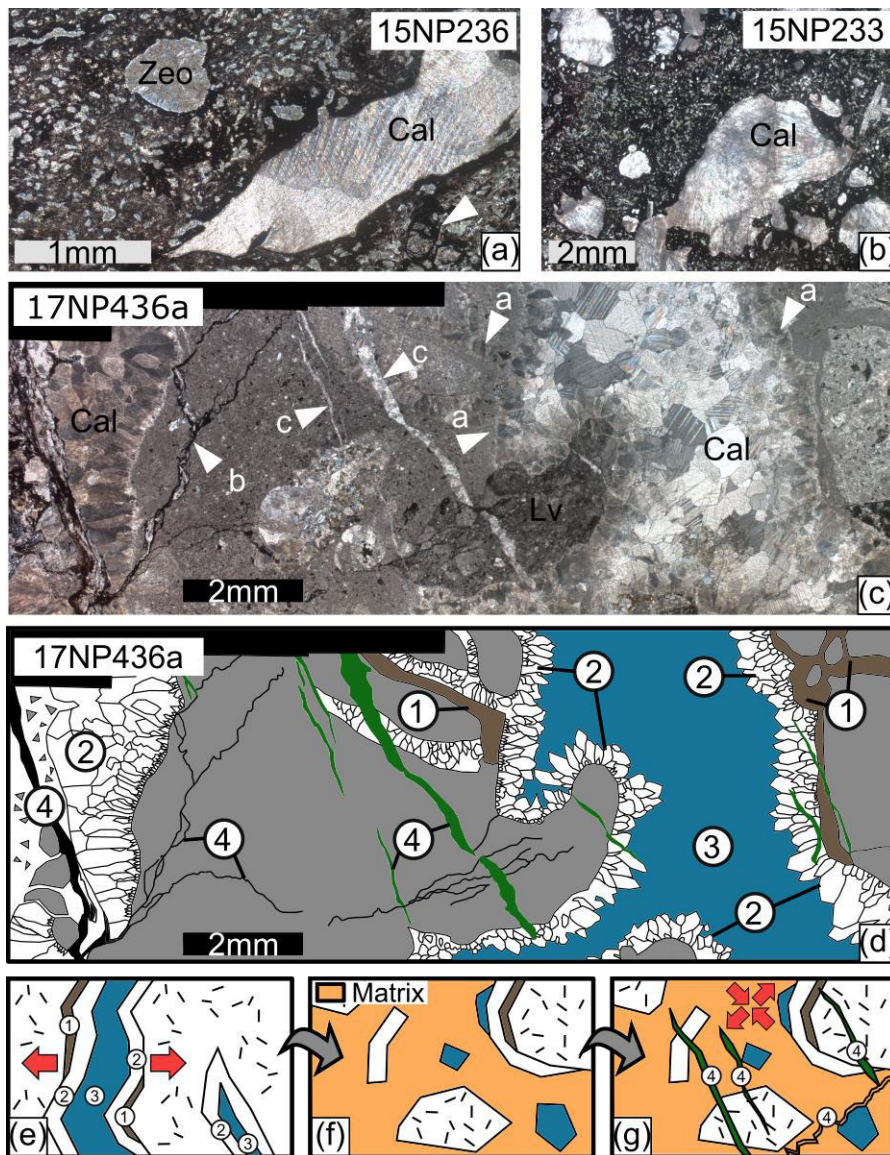


Figure 3: Typical calcite-filled vesicles from sample 15NP236 (a), in this case with spary calcite and zeolite mineralization. The white arrow marks preserved perlitic structures. Botryoidal calcite was found in both amygdaloid-basalt samples, the example in (b) is from 15NP233. Figure 3c shows a thin section photograph of sample 17NP436a. White arrows indicate radial fibrous calcite (a), dark stylolites (b), calcite filled fissures (c). Figure 3a, b, c under crossed polarized light. Figure 3d shows a schematic sketch of microphotograph Figure 3c, delineating a sequence of 4 events: (1) formation of hydrothermal clay, (2) precipitation of fibrous-radial calcite along the walls of brecciated volcanic rock fragments, (3) late-stage equant calcite formation, (4) pressure solution and formation of stylolites (dark lines) and reprecipitation of dissolved calcite in fissures (green). Areas 2 and 3 are targets for laser ablation. In figures (e)-(f) a schematic sequence of events leading to the formation of the basaltic breccias is sketched. (e) Fracturing of the basaltic rock and formation of clay (1) and calcite cement phases (2) and (3). (f) disarticulation and sedimentation of debris containing isolated calcite cement fragments. (g) late stage pressure solution and fissure formation of phase (4). Red arrows schematically indicate stress regime.

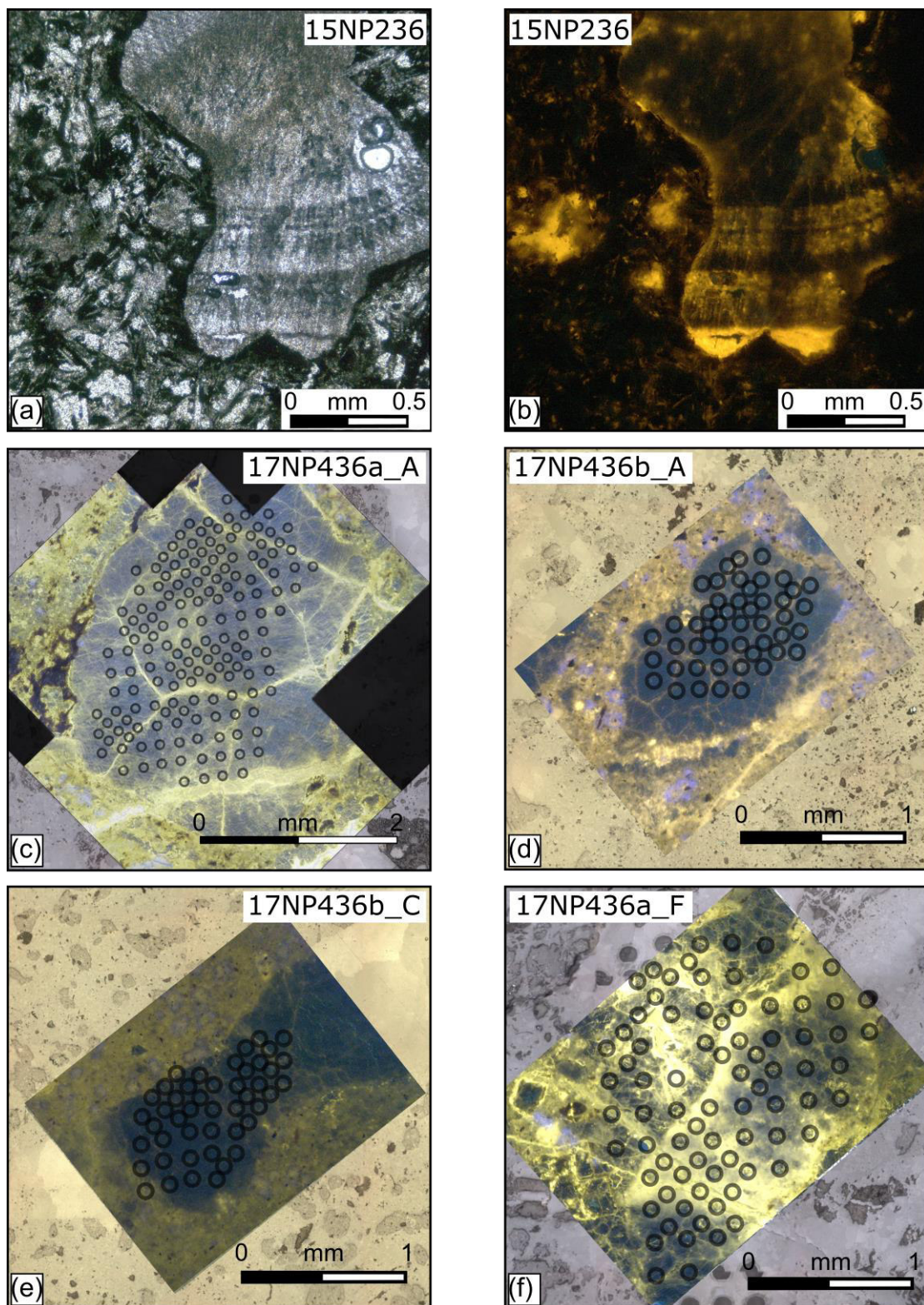
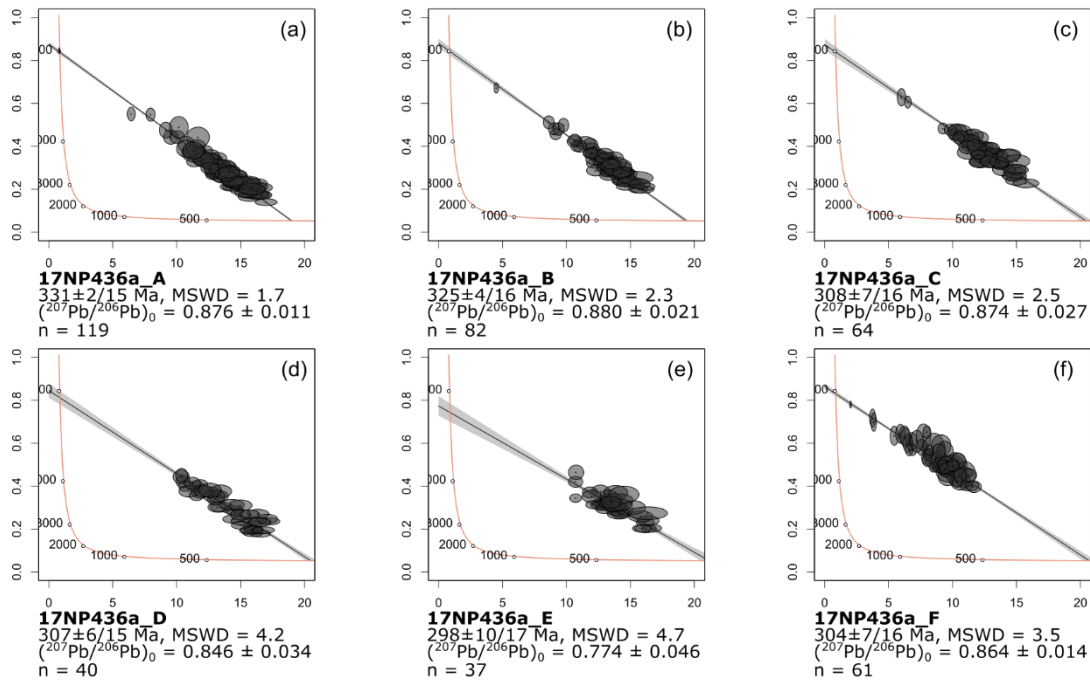


Figure 4: Microphotographs under plain light (a) and cathodoluminescence (b) of an exemplary vesicle from sample 15NP236 show primary botryoidal structure of the calcite. Primary calcite seems non-luminescent to dull-luminescent. Cathodoluminescence images of ablation areas 17NP436a_A (c), 17NP436b_A (d) and 17NP436b_C (e) show relatively homogenous non-luminescent calcite cement fragments with a small portion of bright yellow veins. The calcite cement fragments are embedded in a dull-yellow luminescent volcaniclastic matrix. All three samples yielded high quality calcite U-Pb ages ($MSWD < 2$). Ablation area 17NP436a_F (f), which has a high portion of bright yellow calcite, yielded a less precise age ($MSWD = 3.5$). Ablation spots for geochemistry and U-Pb dating are marked with grey circles.

Basalt breccia sample 17NP436a



Basalt breccia sample 17NP436b

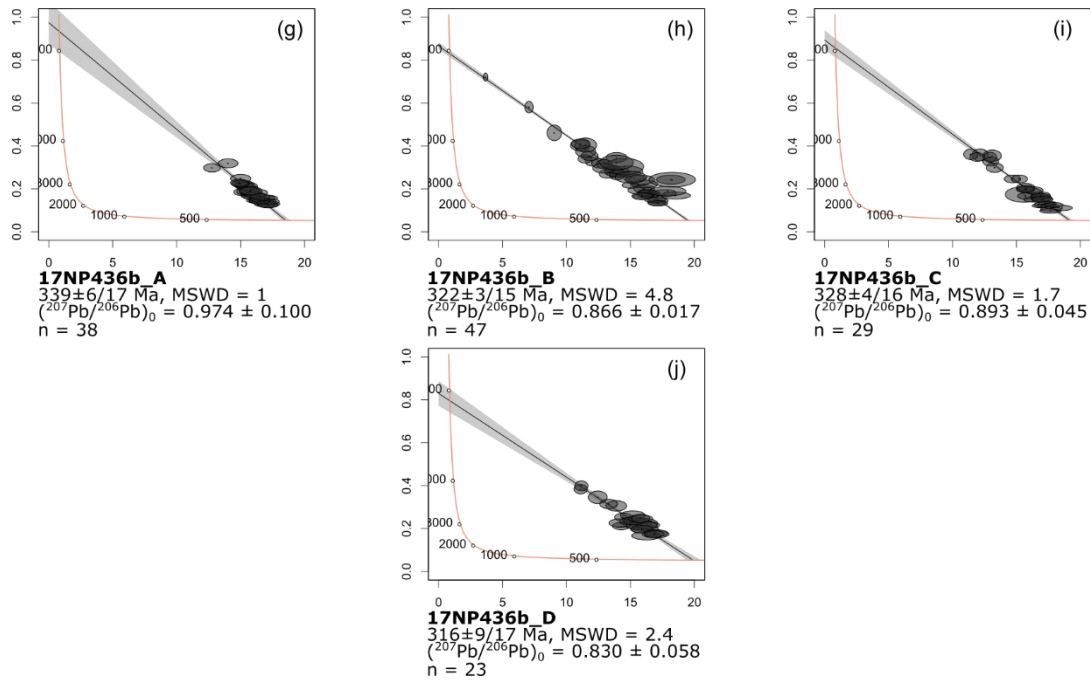
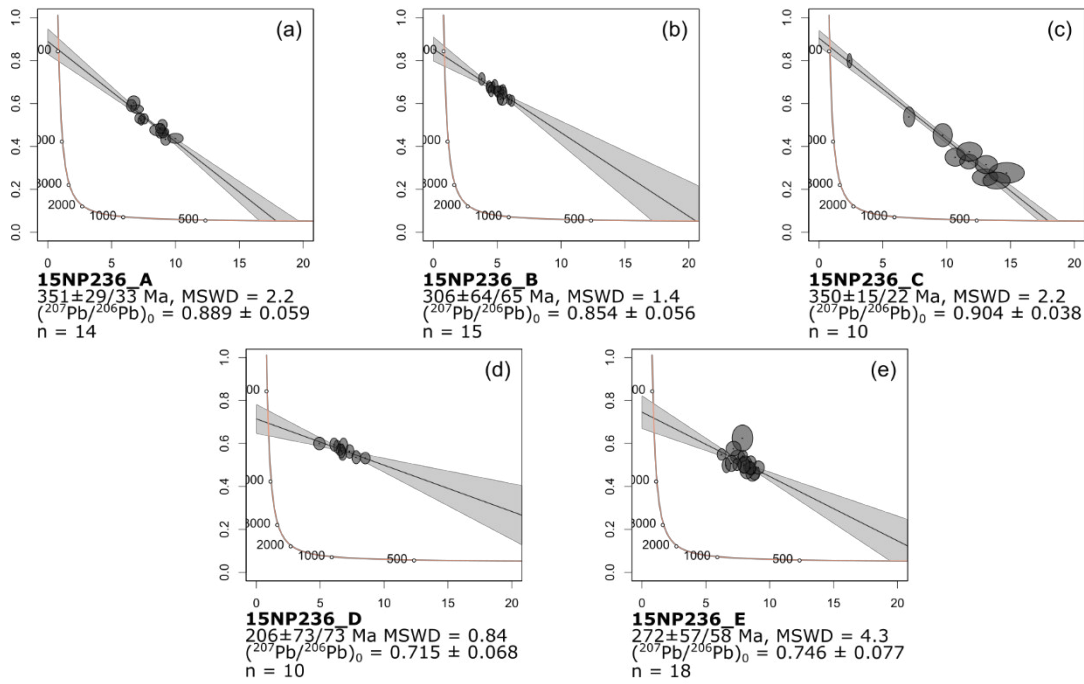


Figure 5: Tera-Wasserburg plots of ablation area ages on basalt breccia samples 17NP436a and 17NP436b. All errors are given as 2σ .

Vesicular basalt sample 15NP236



Vesicular basalt sample 15NP233

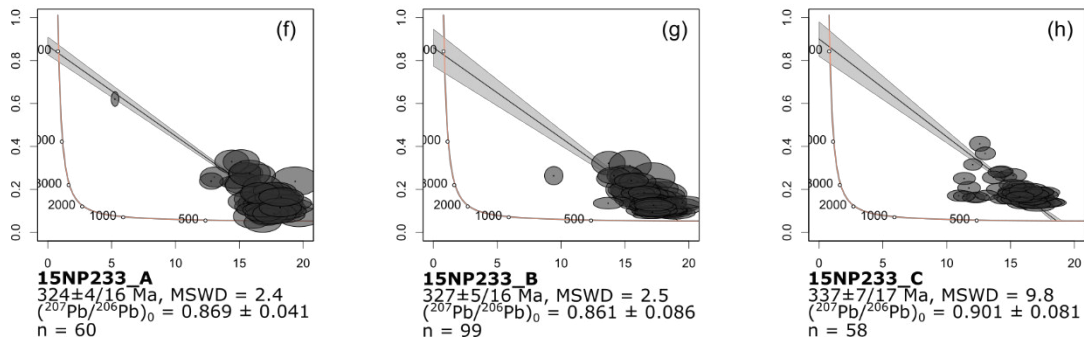


Figure 6: Tera-Wasserburg plots of ablation area ages on vesicular basalt samples 15NP236 and 15NP233. All errors are given as 2σ .

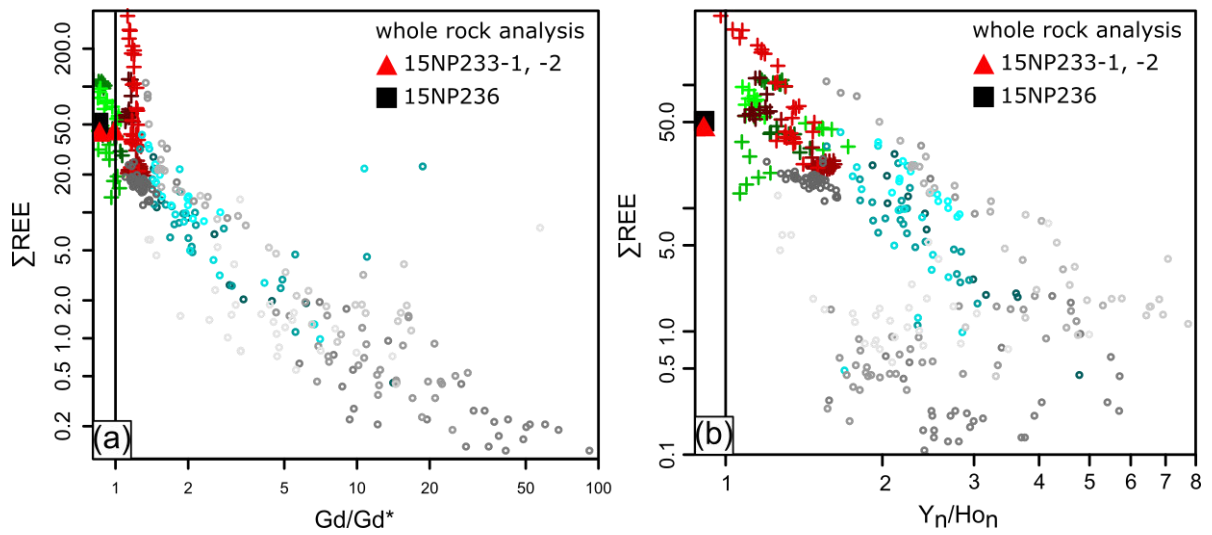


Figure 7: (a) Mixing trend between high total REE—negative Gd/Gd^* and low total REE—positive Gd/Gd^* composition. (b) Higher Y_n/Ho_n values correlate with low total REE. Y and Ho normalized against chondrite values of Anders and Grevesse (1989). (e, f) + -15NP233, -236, o -17NP436A, -B; color-code see Appendix A.

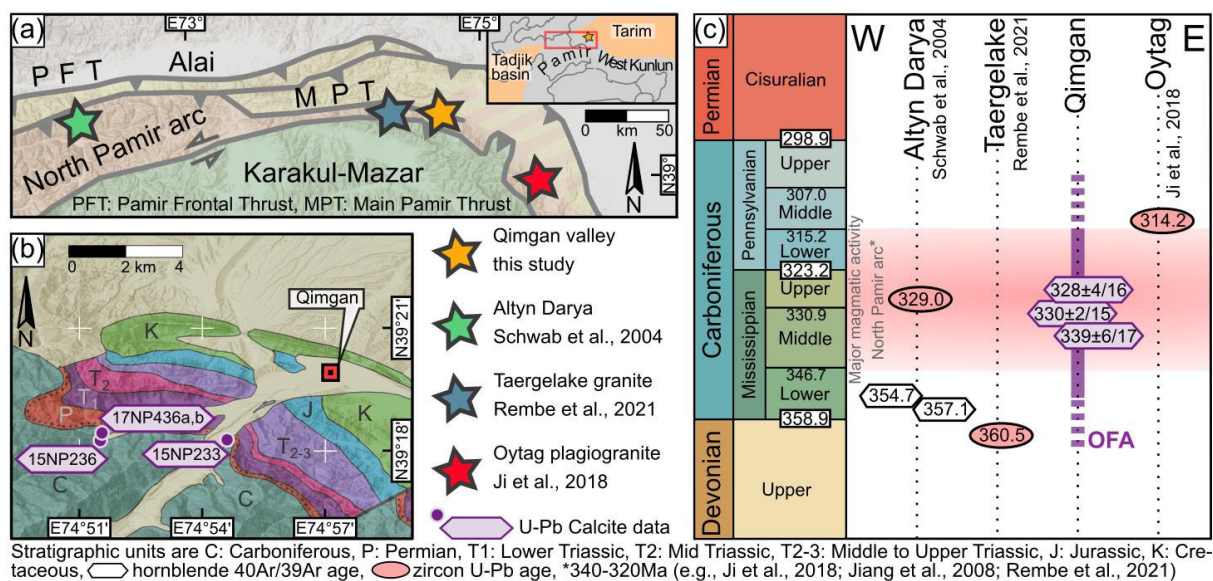


Figure 8: (a) Map of the northeastern Pamir with location of radiometric ages for the North Pamir arc volcanic rocks, shown in c. (b) Detailed field locations of samples in the Qimgan valley (map after Henan Institute of Geological Survey (2014)). There is a sedimentary hiatus between the Middle Pennsylvanian and the Guadalupian (Rembe et al., 2021). (c) Overview of selected literature data and newly obtained data for OFA of the North Pamir Carboniferous arc. Stratigraphic table and ages according to the International Chronostratigraphic Chart (Cohen et al., 2020).

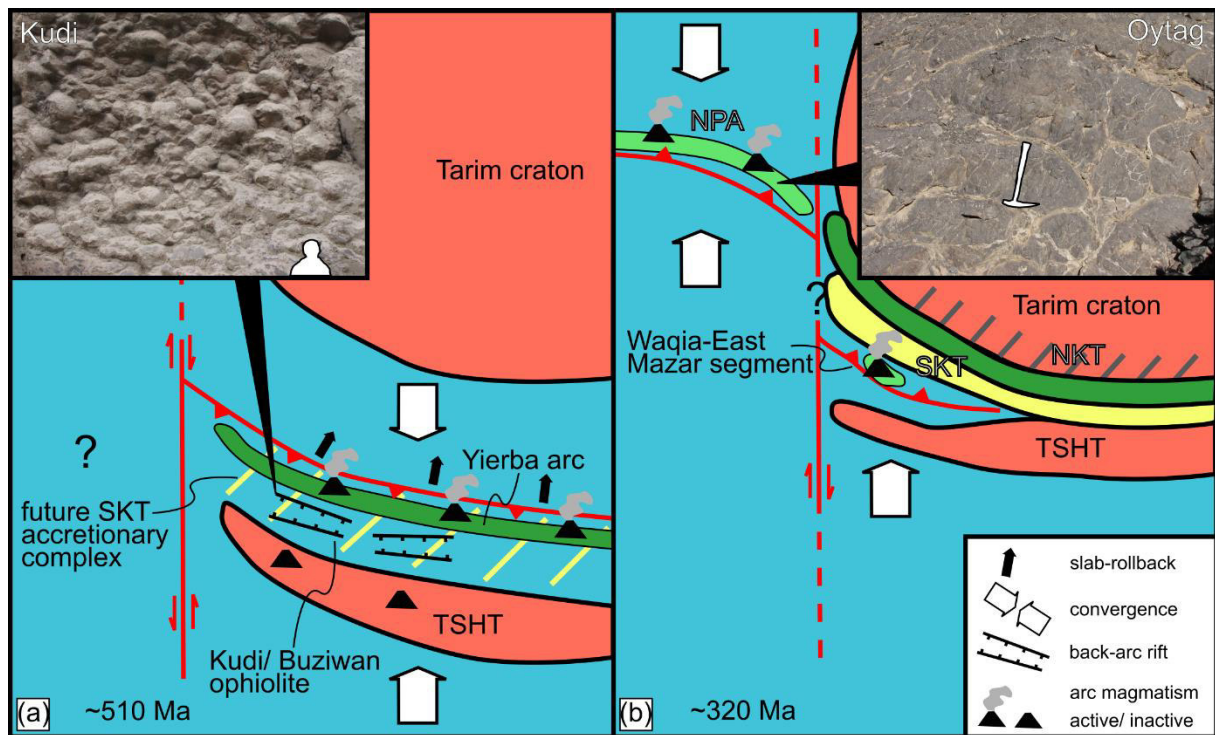


Figure 9: (a) Paleogeographic situation in the mid-Cambrian: The roll-back of the Proto-Tethys slab caused the formation of the Kudi ophiolite, exposed in the Buziwan valley (Wang et al., 2021). (b) Paleogeographic situation in the late Mississippian: The North Pamir arc formed along an intra-oceanic subduction zone (Jiang et al., 2008) forming the Oyttag segment in its eastern branch. Subduction-related Waqia granite (Tang et al., 2020) and East Mazar granite (Li et al., 2006), both today part of tectonic slivers, suggest the presence of a remnant oceanic basin between Tianshuihai and the South Kunlun Terrane accretionary complex, as suggested by Zhang et al. (2018). Small photographs show pillow basalts in the Kudi section (in a) and Oyttag near Qimgan (in b). SKT-South Kunlun Terrane, TSHT-Tianshuihai Terrane, NPA-North Pamir volcanic arc, NKT-North Kunlun Terrane.

13 REFERENCES

- Alibo, D. S. and Nozaki, Y.: Rare earth elements in seawater: particle association, shale-normalization, and Ce oxidation, *Geochimica et Cosmochimica Acta*, 63, 363–372, 1999.
- Anders, E. and Grevesse, N.: Abundances of the elements: Meteoritic and solar, *Geochimica et Cosmochimica Acta*, 53, 197–214, 1989.
- Baar, H. J. de, Brewer, P. G., and Bacon, M. P.: Anomalies in rare earth distributions in seawater: Gd and Tb, *Geochimica et Cosmochimica Acta*, 49, 1961–1969, [https://doi.org/10.1016/0016-7037\(85\)90090-0](https://doi.org/10.1016/0016-7037(85)90090-0), 1985.
- Bazhenov, M. L. and Burtman, V. S.: The kinematics of the Pamir arc: *Geotectonics*, v. 16, 1982.
- Boynnton, W. V.: Cosmochemistry of the rare earth elements: meteorite studies, in: *Developments in geochemistry*, Elsevier, 63–114, 1984.
- Burtman, V. S., Peive, A. V., and Ruzhentsev, S. V.: The main lateral faults of the Tien Shan and Pamir, *Faults and Horizontal Movements of the Earth's Crust*, 152–172, 1963.
- Burtman, V. S. and Molnar, P. H.: Geological and geophysical evidence for deep subduction of continental crust beneath the Pamir, *Geological Society of America*, 1993.
- Cohen, K., Harper, D. A., and Gibbard, P.: International Chronostratigraphic Chart (v 2020/03), International Commission on Stratigraphy. Hentet fra <https://stratigraphy.org/icschart/ChronostratChart2020-03.pdf>, 2020.
- Coogan, L. A. and Gillis, K. M.: Low-Temperature Alteration of the Seafloor: Impacts on Ocean Chemistry, *Annu. Rev. Earth Planet. Sci.*, 46, 21–45, 2018.
- Coogan, L. A., Parrish, R. R., and Roberts, N. M. W.: Early hydrothermal carbon uptake by the upper oceanic crust: Insight from in situ U-Pb dating, *Geol*, 44, 147–150, 2016.
- Debruyne, D., Hulsbosch, N., and Muchez, P.: Unraveling rare earth element signatures in hydrothermal carbonate minerals using a source–sink system, *Ore Geology Reviews*, 72, 232–252, 2016.
- Fisher, A. T. and Becker, K.: Channelized fluid flow in oceanic crust reconciles heat-flow and permeability data, *Nature*, 403, 71–74, 2000.
- Godeau, N., Deschamps, P., Guihou, A., Leonide, P., Tendil, A., Gerdes, A., Hamelin, B., and Girard, J.-P.: U-Pb dating of calcite cement and diagenetic history in microporous carbonate reservoirs: Case of the Urgonian Limestone, France, *Geology*, 46, 247–250, 2018.
- Gonzalez, L. A. and Carpenite, S. J.: Inorganic Calcite Morphology: Roles of Fluid Chemistry and Fluid Flow, *SEPM JSR*, Vol. 62, 1992.
- Harlov, D. E. and Austrheim, H. (Eds.): *Metasomatism and the chemical transformation of rock: The role of fluids in terrestrial and extraterrestrial processes* / Daniel E. Harlov, Håkon Austrheim [editors], Lecture notes in earth system sciences, 2193-8571, Springer, Heidelberg, London, 2013.
- Heath, M., Phillips, D., and Matchan, E. L.: An evidence-based approach to accurate interpretation of $^{40}\text{Ar}/^{39}\text{Ar}$ ages from basaltic rocks, *Earth and Planetary Science Letters*, 498, 65–76, 2018.

507 Henan Institute of Geological Survey: The 1:250000 Geological Map of the Peoples Republic of China
508 (J43C001002, Kuergan), China Coal Xi' and Map Printing Co., Ltd., 2014.

509 Honnorez, J.: Hydrothermal alteration vs. ocean-floor metamorphism. A comparison between two case histories:
510 the TAG hydrothermal mound (Mid-Atlantic Ridge) vs. DSDP/ODP Hole 504B (Equatorial East Pacific),
511 *Comptes Rendus Geoscience*, 335, 781–824, 2003.

512 Horstwood, M. S. A., Košler, J., Gehrels, G., Jackson, S. E., McLean, N. M., Paton, C., Pearson, N. J., Sircombe,
513 K., Sylvester, P., and Vermeesch, P.: Community-derived standards for LA-ICP-MS U-(Th-) Pb
514 geochronology–Uncertainty propagation, age interpretation and data reporting, *Geostandards and*
515 *Geoanalytical Research*, 40, 311–332, 2016.

516 Howard, D. L., Jonge, M. D. de, Afshar, N., Ryan, C. G., Kirkham, R., Reinhardt, J., Kewish, C. M., McKinlay,
517 J., Walsh, A., and Divitcos, J.: The XFM beamline at the Australian Synchrotron, *Journal of Synchrotron*
518 *Radiation*, 27, 1447–1458, 2020.

519 Ji, W. H., Chen, S. J., Li, R. S., He, S. P., Zhao, Z. M., and Pan, X. P.: The origin of Carboniferous-Permian
520 magmatic rocks in Oyttag area, West Kunlun: Back-arc basin?, *Acta Petrologica Sinica*, 34, 2393–2409,
521 2018.

522 Jiang, C. F.: Opening-closing tectonics of Kunlun Mountains, *Geol. Memoirs. MGMR*, 12, 1–224, 1992.

523 Jiang, Y.-H., Liao, S.-Y., Yang, W.-Z., and Shen, W.-Z.: An island arc origin of plagiogranites at Oyttag, western
524 Kunlun orogen, northwest China: SHRIMP zircon U–Pb chronology, elemental and Sr–Nd–Hf isotopic
525 geochemistry and Paleozoic tectonic implications, *Lithos*, 106, 323–335,
526 <https://doi.org/10.1016/j.lithos.2008.08.004>, 2008.

527 Kang, L., Xiao, P. X., Gao, X. F., Wang, C., Yang, Z. C., and Xi, R. G.: Geochemical characteristics,
528 petrogenesis and tectonic setting of oceanic plagiogranites belt in the northwestern margin of western
529 Kunlun, *Acta Petrologica Sinica*, 31, 2566–2582, 2015.

530 Konopelko, D., Biske, Y. S., Kullerud, K., Ganiev, I., Seltmann, R., Brownscombe, W., Mirkamalov, R., Wang,
531 B., Safonova, I., and Kotler, P.: Early Carboniferous metamorphism of the Neoproterozoic South Tien Shan-
532 Karakum basement: New geochronological results from Baisun and Kyzylkum, Uzbekistan, *Journal of*
533 *Asian Earth Sciences*, 177, 275–286, 2019.

534 Lan, Z., Roberts, N. M. W., Zhou, Y., Zhang, S., Li, Z., and Zhao, T.: Application of in situ U-Pb carbonate
535 geochronology to Stenian-Tonian successions of North China, *Precambrian Research*, 370, 106551, 2022.

536 Li, B., Yao, J., Ji, W. H., Zhang, J., Yin, Z., Chen, G., Lin, X., Zhang, Q., KONG, W., Wang, F., and LIU, X.:
537 Characteristics and zircon SHRIMP U-Pb ages of the arc magmatic rocks in Mazar, southern Yecheng, West
538 Kunlun Mountains., *Geological Bulletin of China*, Z1, 124–132, 2006.

539 Li, Y.-P., Robinson, A. C., Lapen, T. J., Richter, M., and Stevens, M. K.: Muztaghata Dome Miocene Eclogite
540 Facies Metamorphism: A Record of Lower Crustal Evolution of the NE Pamir, *Tectonics*, 39, 2020.

541 Liu, Z., Jiang, Y.-H., Jia, R.-Y., Zhao, P., Zhou, Q., Wang, G.-C., and Ni, C.-Y.: Origin of Middle Cambrian and
542 Late Silurian potassic granitoids from the western Kunlun orogen, northwest China: a magmatic response to
543 the Proto-Tethys evolution, *Miner Petrol*, 108, 91–110, 2014.

544 Mattern, F., Schneider, W., Li, Y., and Li, X.: A traverse through the western Kunlun (Xinjiang, China):
545 Tentative geodynamic implications for the Paleozoic and Mesozoic, *Geol Rundsch*, 85, 705–722, 1996.

546 May, T. W. and Wiedmeyer, R. H.: A table of polyatomic interferences in ICP-MS, *ATOMIC*
547 *SPECTROSCOPY-NORWALK CONNECTICUT-*, 19, 150–155, 1998.

548 Möller, P., Rosenthal, E., Geyer, S., Guttman, J., Dulski, P., Rybakov, M., Zilberbrand, M., Jahnke, C., and
549 Flexer, A.: Hydrochemical processes in the lower Jordan valley and in the Dead Sea area, *Chemical*
550 *Geology*, 239, 27–49, 2007.

551 Nuriel, P., Craddock, J., Kylander-Clark, A. R. C., Uysal, I. T., Karabacak, V., Dirik, R. K., Hacker, B. R., and
552 Weinberger, R.: Reactivation history of the North Anatolian fault zone based on calcite age-strain analyses,
553 *Geology*, 47, 465–469, 2019.

554 Pan, Y.: Discovery and evidence of the fifth suture zone of Qinghai-xizang plateau, *Chinese Journal of*
555 *Geophysics*, 2, 1994.

556 Paton, C., Hellstrom, J., Paul, B., Woodhead, J., and Hergt, J.: Iolite: Freeware for the visualisation and
557 processing of mass spectrometric data, *Journal of Analytical Atomic Spectrometry*, 26, 2508–2518, 2011.

558 Perry, E. P. and Gysi, A. P.: Rare Earth Elements in Mineral Deposits: Speciation in Hydrothermal Fluids and
559 Partitioning in Calcite, *Geofluids*, 2018, 1–19, <https://doi.org/10.1155/2018/5382480>, available at:
560 <https://www.hindawi.com/journals/geofluids/2018/5382480/>, 2018.

561 Pringle, M. S.: Age Progressive Volcanism in the Musicians Seamounts: A Test of the Hot Spot Hypothesis for
562 the Late Cretaceous Pacific, in: *The Mesozoic Pacific: Geology, Tectonics, and Volcanism*, American
563 *Geophysical Union (AGU)*, 187–215, <https://doi.org/10.1029/GM077p0187>, 2013.

564 Rasbury, E. T., Present, T. M., Northrup, P., Tappero, R. V., Lanzirotti, A., Cole, J. M., Wooton, K. M., and
565 Hatton, K.: Tools for uranium characterization in carbonate samples: case studies of natural U–Pb
566 geochronology reference materials, *Geochronology*, 3, 103–122, <https://doi.org/10.5194/gchron-3-103-2021>,
567 2021.

568 Rembe, J., Sobel, E. R., Kley, J., Zhou, R., Thiede, R., and Chen, J.: The Carboniferous Arc of the North Pamir,
569 *Lithosphere*, 2021, <https://doi.org/10.2113/2021/6697858>, available at:
570 [https://pubs.geoscienceworld.org/gsa/lithosphere/article/2021/1/6697858/594514/The-Carboniferous-Arc-of-](https://pubs.geoscienceworld.org/gsa/lithosphere/article/2021/1/6697858/594514/The-Carboniferous-Arc-of-the-North-Pamir)
571 [the-North-Pamir](https://pubs.geoscienceworld.org/gsa/lithosphere/article/2021/1/6697858/594514/The-Carboniferous-Arc-of-the-North-Pamir), 2021.

572 Roberts, N. M. W., Žák, J., Vacek, F., and Sláma, J.: No more blind dates with calcite: Fluid-flow vs. fault-slip
573 along the Očkov thrust, Prague Basin, *Geoscience Frontiers*, 12, 101143, 2021.

574 Roberts, N. M. W., Rasbury, E. T., Parrish, R. R., Smith, C. J., Horstwood, M. S. A., and Condon, D. J.: A
575 calcite reference material for LA-ICP-MS U-Pb geochronology, *Geochemistry, Geophysics, Geosystems*,
576 18, 2807–2814, <https://doi.org/10.1002/2016GC006784>, available at:
577 <http://onlinelibrary.wiley.com/doi/10.1002/2016GC006784/full>, 2017.

578 Ruzhentsev, S., Pospelov, I., and Sukhanov, A. N.: Tectonics of Khalaihumb-Sauksau zone of the North Pamir,
579 *Geotectonics*, 4, 68–80, 1977.

Schwab, M., Ratschbacher, L., Siebel, W., McWilliams, M., Minaev, V., Lutkov, V., Chen, F., Stanek, K.,
 Nelson, B., Frisch, W., and Wooden, J. L.: Assembly of the Pamirs: Age and origin of magmatic belts from
 the southern Tien Shan to the southern Pamirs and their relation to Tibet, *Tectonics*, 23, n/a-n/a, 2004.

Spivack, A. J. and Staudigel, H.: Low-temperature alteration of the upper oceanic crust and the alkalinity budget
 of seawater, *Chemical Geology*, 115, 239–247, 1994.

Staudigel, H., Plank, T., White, B., and Schmincke, H.-U.: Geochemical Fluxes During Seafloor Alteration of
 the Basaltic Upper Oceanic Crust: DSDP Sites 417 and 418, in: *Subduction top to bottom*, edited by:
 Bebout, G. E., Scholl, D. W., and Kirby, S. H., American Geophysical Union, Washington, 19–38,
<https://doi.org/10.1029/GM096p0019>, 2013.

Su, A., Chen, H., Feng, Y., Zhao, J., Nguyen, A. D., Wang, Z., and Long, X.: Dating and characterizing primary
 gas accumulation in Precambrian dolomite reservoirs, Central Sichuan Basin, China: Insights from
 pyrobitumen Re-Os and dolomite U-Pb geochronology, *Precambrian Research*, 350, 105897, 2020.

Talbi, E. H. and Honnorez, J.: Low-temperature alteration of mesozoic oceanic crust, *Ocean Drilling Program
 Leg 185, Geochem. Geophys. Geosyst.*, 4, 2003.

Tang, W., Wang, S., Liu, Y., Yao, X., and Li, M.: Origin of Carboniferous intra-oceanic arc granitoids from the
 eastern Pamir and implications for the Paleo-Tethyan ocean, 2020.

Vanghi, V., Borsato, A., Frisia, S., Howard, D. L., Gloy, G., Hellstrom, J., and Bajo, P.: High-resolution
 synchrotron X-ray fluorescence investigation of calcite coralloid speleothems: Elemental incorporation and
 their potential as environmental archives, *Sedimentology*, 66, 2661–2685, 2019.

Vermeesch, P.: IsoplotR: a free and open toolbox for geochronology, *Geoscience Frontiers*, 9, 1479–1493, 2018.

Voigt, M., Mavromatis, V., and Oelkers, E. H.: The experimental determination of REE partition coefficients in
 the water-calcite system, *Chemical Geology*, 462, 30–43, 2017.

Waagstein, R., Guise, P., and Rex, D.: K/Ar and $^{39}\text{Ar}/^{40}\text{Ar}$ whole-rock dating of zeolite facies
 metamorphosed flood basalts: the upper Paleocene basalts of the Faroe Islands, NE Atlantic, *Geological
 Society, London, Special Publications*, 197, 219–252, <https://doi.org/10.1144/GSL.SP.2002.197.01.09>,
 2002.

Wang, P., Zhao, G., Liu, Q., Han, Y., Zhang, Y., Yao, J., and Yu, S.: Slab-controlled progressive evolution of
 the Kudi back-arc ophiolite in response to the rollback of the Proto-Tethys oceanic slab, in Western Kunlun,
 NW Tibetan Plateau, *Lithos*, 380–381, 105877, 2021.

Wang, P., Zhao, G., Han, Y., Liu, Q., Yao, J., Yu, S., and Li, J.: Timing of the final closure of the Proto-Tethys
 Ocean: Constraints from provenance of early Paleozoic sedimentary rocks in West Kunlun, NW China,
Gondwana Research, 2020.

Woodhead, J. D. and Hergt, J. M.: Strontium, neodymium and lead isotope analyses of NIST glass certified
 reference materials: SRM 610, 612, 614, *Geostandards Newsletter*, 25, 261–266, 2001.

Xiao, W. J., Windley, B. F., Liu, D. Y., Jian, P., Liu, C. Z., Yuan, C., and Sun, M.: Accretionary tectonics of the
 Western Kunlun Orogen, China: A Paleozoic–Early Mesozoic, long-lived active continental margin with
 implications for the growth of Southern Eurasia, *The Journal of Geology*, 113, 687–705, 2005.

- Xiao, W. J., Windley, B. F., Chen, H. L., Zhang, G. C., and Li, J. L.: Carboniferous-Triassic subduction and accretion in the western Kunlun, China: Implications for the collisional and accretionary tectonics of the northern Tibetan Plateau, *Geology*, 30, 295–298, 2002.
- Yang, P., Wu, G., Nuriel, P., Nguyen, A. D., Chen, Y., Yang, S., Feng, Y., Ren, Z., and Zhao, J.: In situ LA-ICPMS UPb dating and geochemical characterization of fault-zone calcite in the central Tarim Basin, northwest China: Implications for fluid circulation and fault reactivation, *Chemical Geology*, 568, 120125, 2021.
- Yin, J., Xiao, W., Sun, M., Chen, W., Yuan, C., Zhang, Y., Wang, T., Du, Q., Wang, X., and Xia, X.: Petrogenesis of Early Cambrian granitoids in the western Kunlun orogenic belt, Northwest Tibet: Insight into early stage subduction of the Proto-Tethys Ocean, *Bulletin*, 132, 2221–2240, 2020.
- Yuan, C., Sun, M., Zhou, M., Zhou, H., Xiao, W., and Li, J.: Tectonic Evolution of the West Kunlun: Geochronologic and Geochemical Constraints from Kudi Granitoids, *International Geology Review*, 44, 653–669, <https://doi.org/10.2747/0020-6814.44.7.653>, 2002.
- Zhang, C., Yu, H., Ye, H., Zhao, Y., and Zhang, D.: Aoyitake plagiogranite in western Tarim Block, NW China: Age, geochemistry, petrogenesis and its tectonic implications, *Science in China Series D: Earth Sciences*, 49, 1121–1134, <https://doi.org/10.1007/s11430-006-1121-y>, available at: <https://doi.org/10.1007/s11430-006-1121-y>, 2006.
- Zhang, C.-L., Zou, H.-B., Ye, X.-T., and Chen, X.-Y.: Tectonic evolution of the West Kunlun Orogenic Belt along the northern margin of the Tibetan Plateau: Implications for the assembly of the Tarim terrane to Gondwana, *Geoscience Frontiers*, 2018.

17NP436a

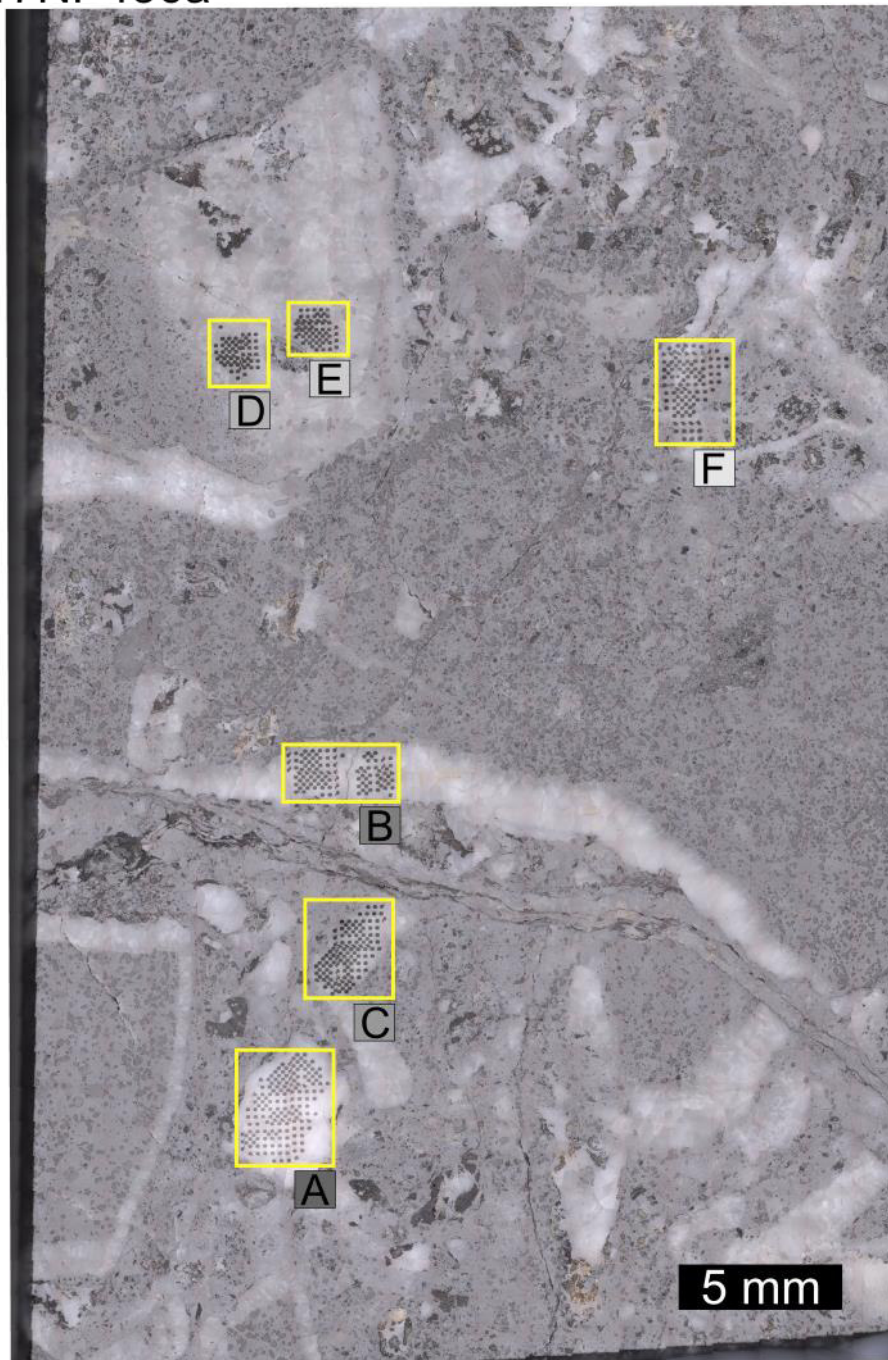


Figure A1. Reflected light image of sample 17NP436a with marked ablation areas. Letter, attached to the yellow boxes, appended to the sample name, labels the ablation areas. Colors of label boxes are consistent with colors of in-text figures.

17NP436b

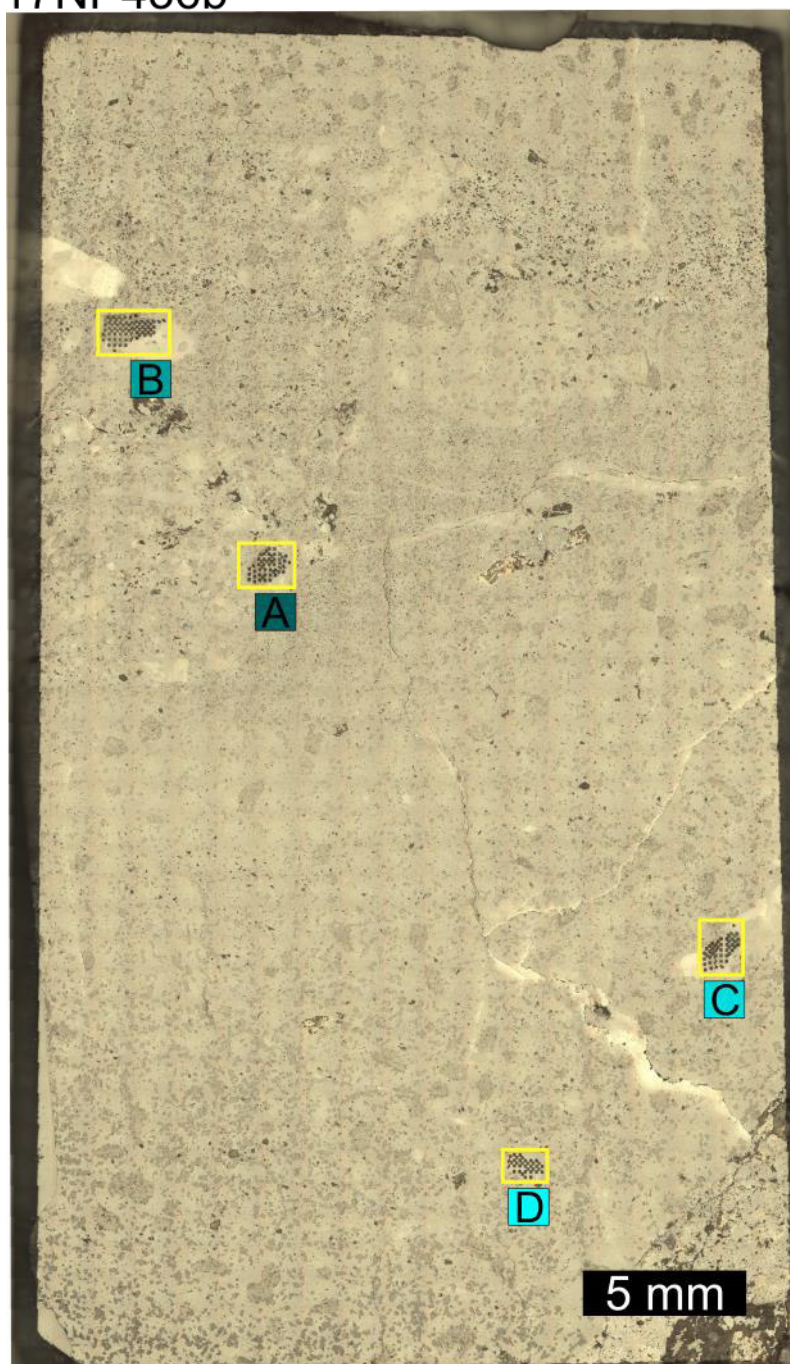


Figure A2. Reflected light image of sample 17NP436b with marked ablation areas. Letter, attached to the yellow boxes, appended to the sample name, labels the ablation areas. Colors of label boxes are consistent with colors of in-text figures.

15NP233

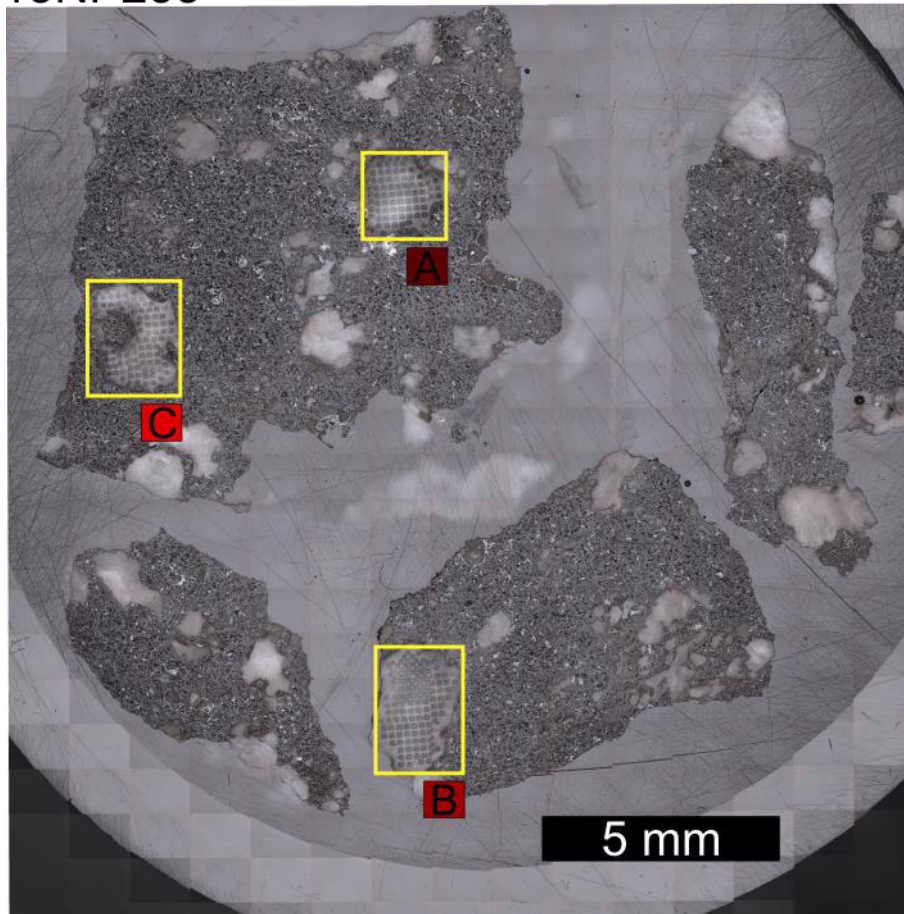


Figure A3. Reflected light image of sample 15NP233 with marked ablation areas. Letter, attached to the yellow boxes, appended to the sample name, labels the ablation areas. Colors of label boxes are consistent with colors of in-text figures.

15NP236

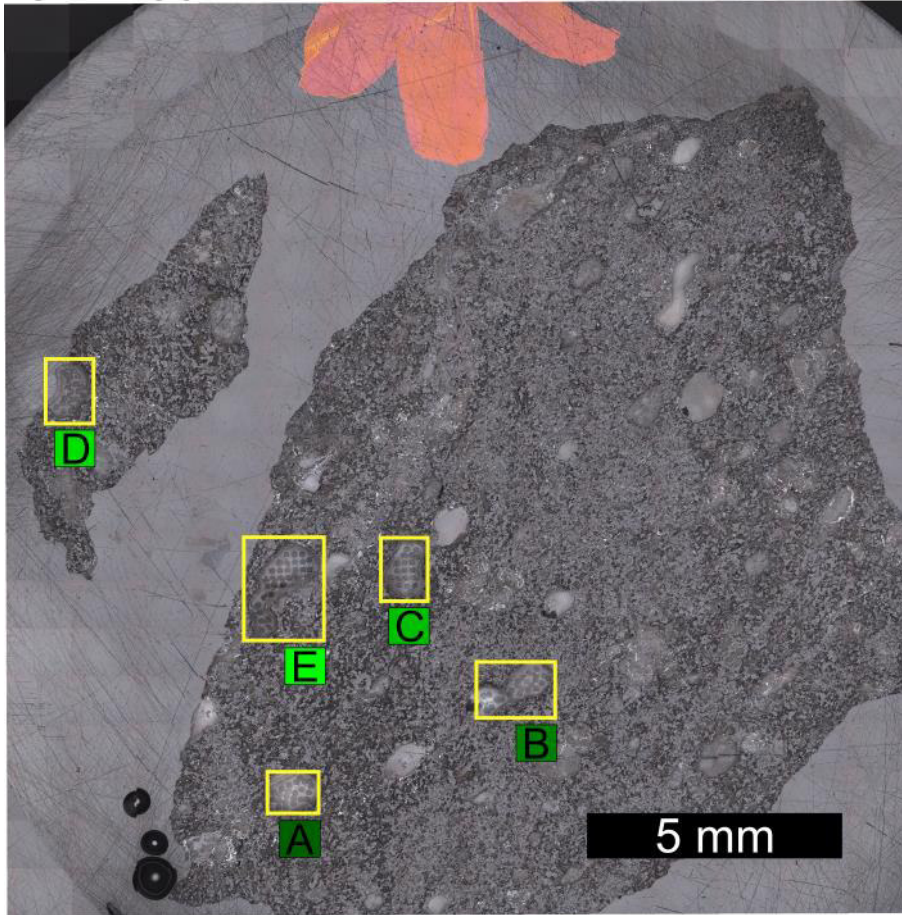
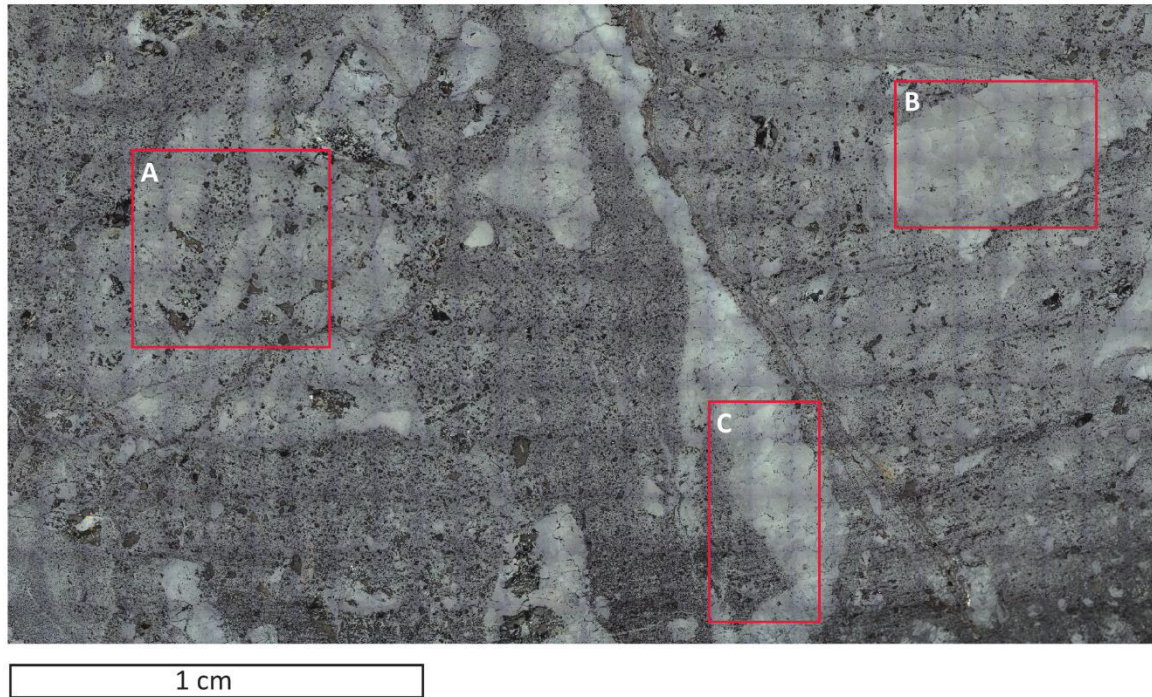


Figure A4. Reflected light image of sample 15NP236 with marked ablation areas. Letter, attached to the yellow boxes, appended to the sample name, labels the ablation areas. Colors of label boxes are consistent with colors of in-text figures.

Appendix B

Reflective light photo



Cross-polarized light photo

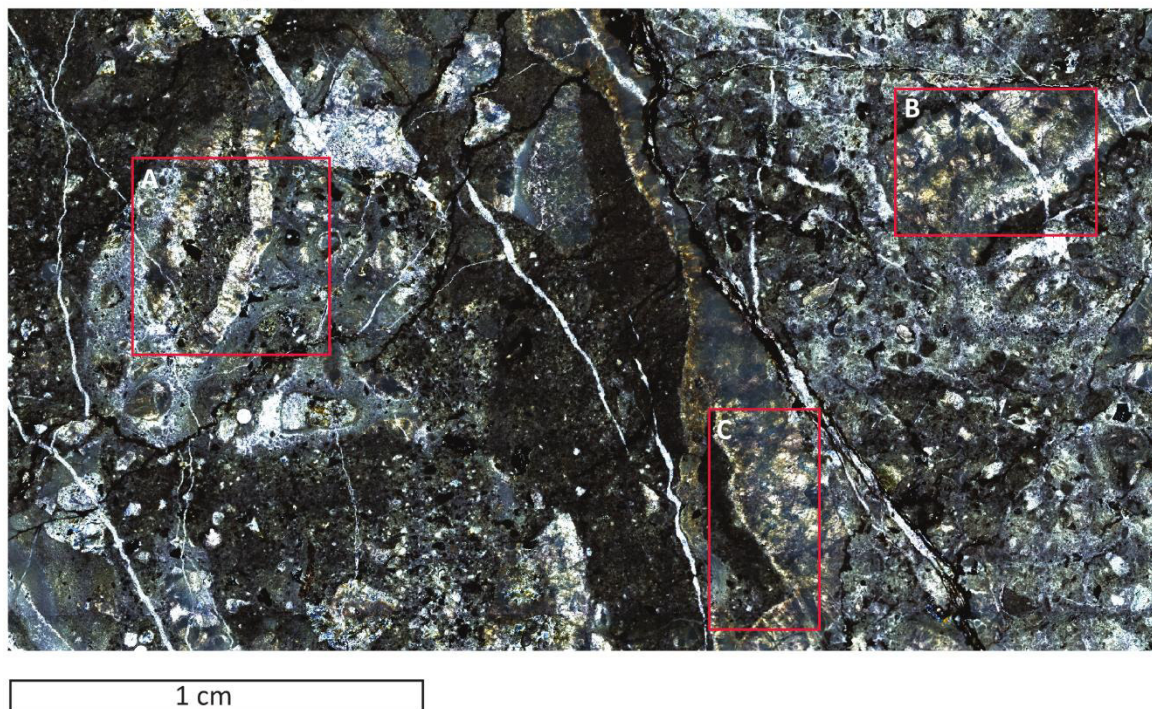
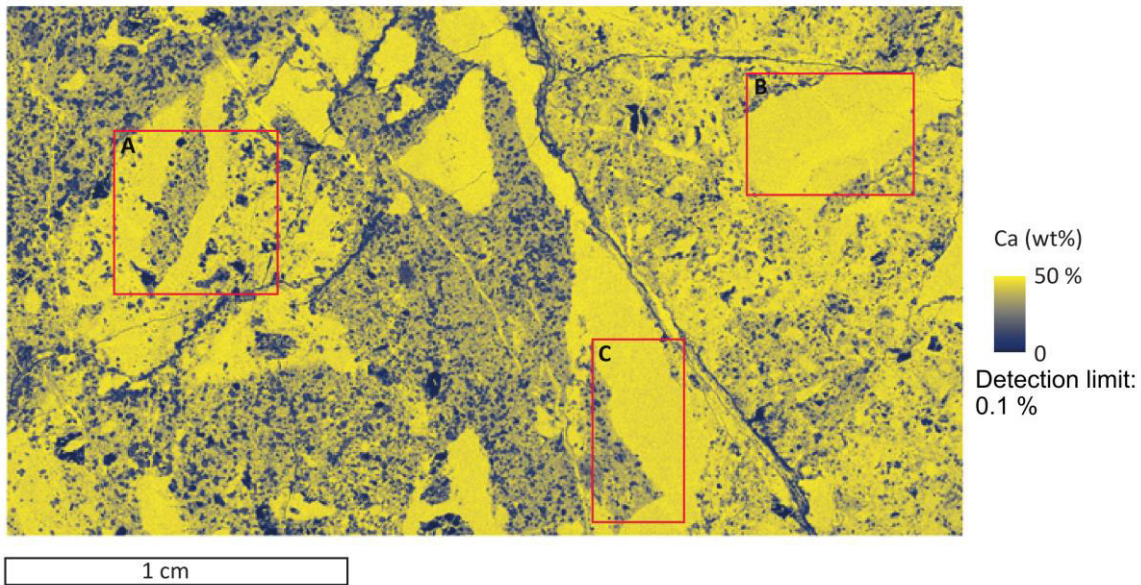


Figure B1. Reflected light image and cross-polarized light image of the investigation area on sample 17NP436a.

Appendix B

Scan 66079 (resolution: 10 μm / pixel; dwell time: 1ms)



Scan 66079 (resolution: 10 μm / pixel; dwell time: 1ms)

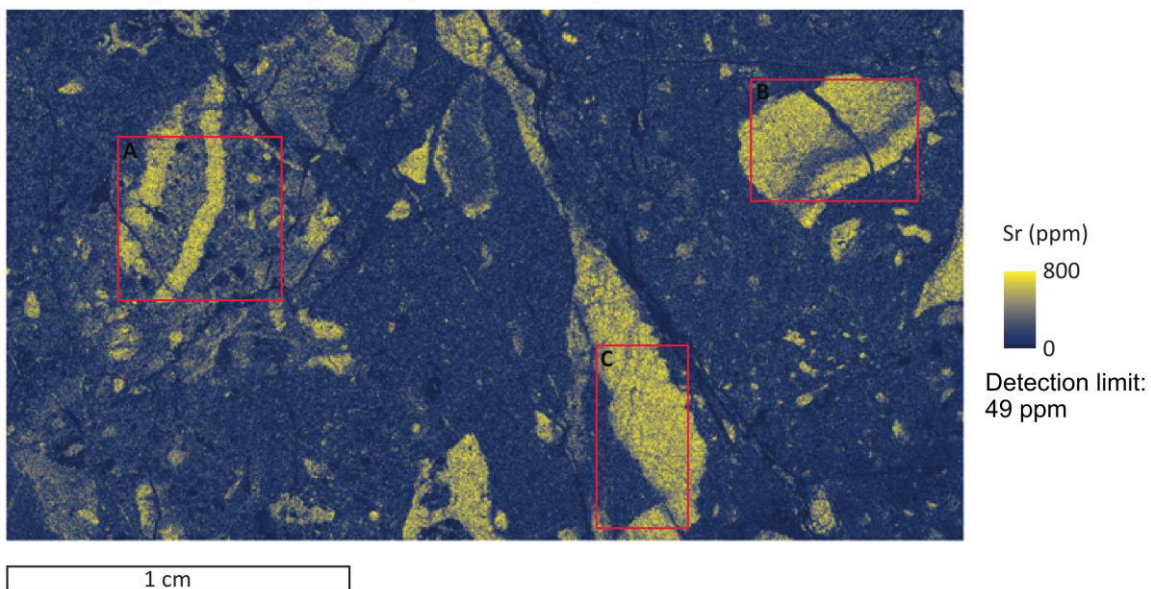


Figure B2. Coarse scan of the investigation areas on sample 17NP436a for Ca and Sr.

Area A shows a rock fragment fringed by radial-fibrous calcite cement. The right fissure shows calcite growing from both walls toward the center, showing lower Sr values in the center of the vein.

Area B shows an isolated fragment of radial-fibrous to equant cement with Sr and Ca zoning. High Sr/ low Ca values occur in the radial-fibrous calcite along the lower-right boundary with an abrupt change to low Sr/ high Ca values in the center that grade into high Sr/ low Ca values in a broad zone along the upper-left boundary. The low Sr/ high Ca values occur at the transition from radial-fibrous to equant calcite crystals. A younger calcite filled fissure crosscuts the calcite cement fragment. Crucial are the much lower Sr values. This fissure formed during tectonic straining of the rock, pressure solution and reprecipitation of calcite.

Area C shows calcite crystals with highest Sr/ lowest Ca values in the center of the single crystals.

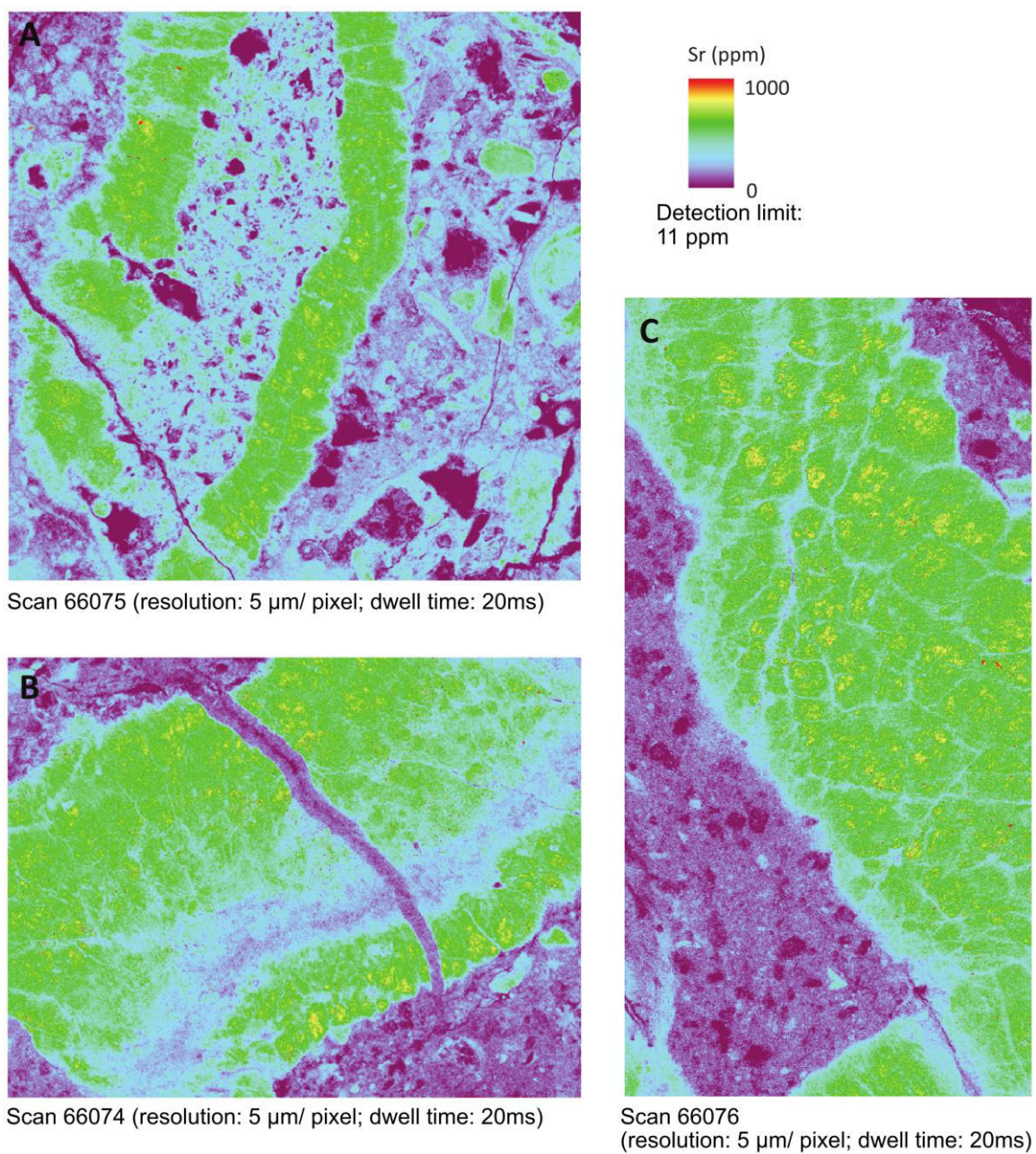


Figure B3. Fine scan of the investigation areas on sample 17NP436a for Sr.

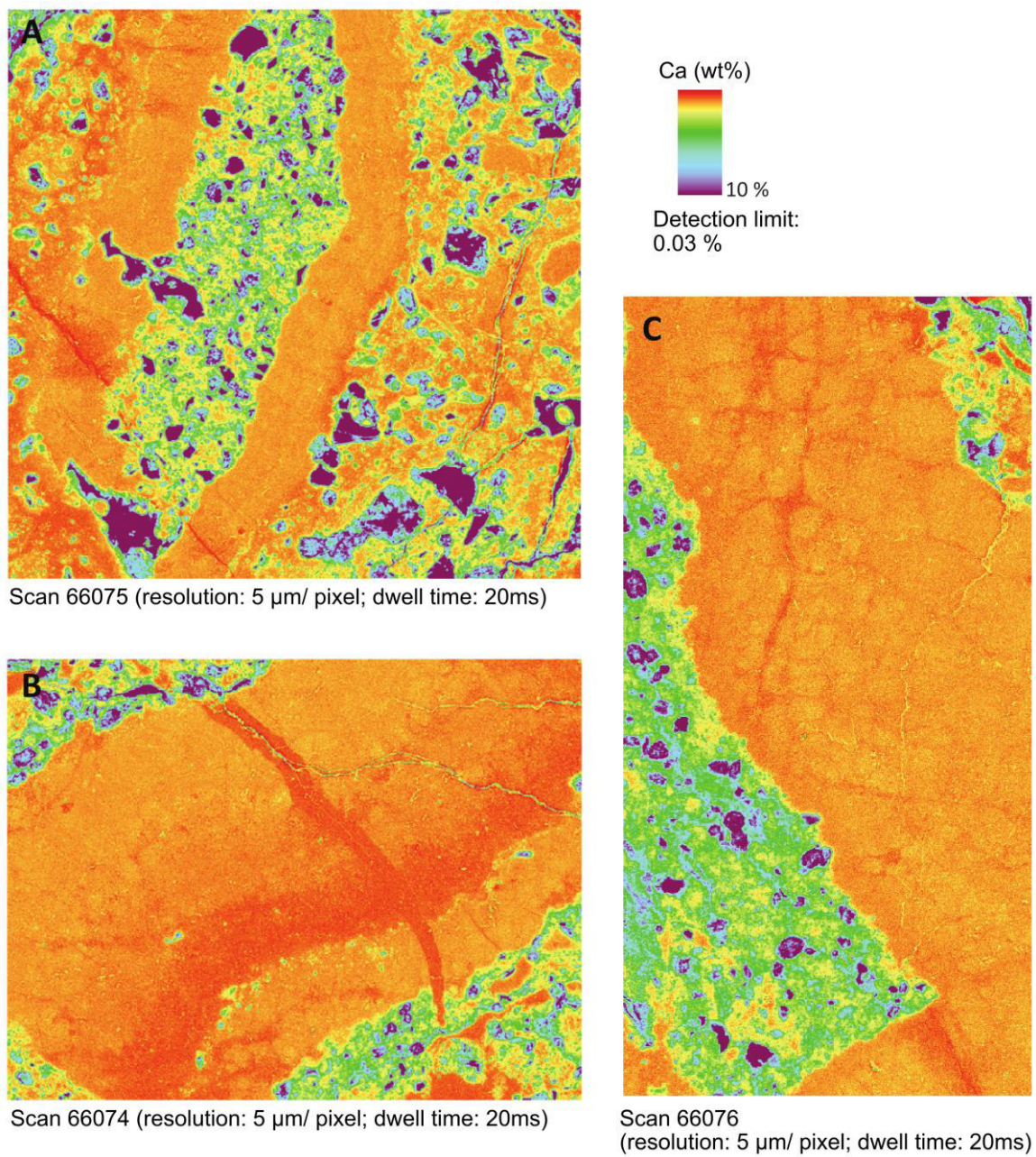


Figure B4. Fine scan of the investigation areas on sample 17NP436a for Ca.

17NP436a basalt breccia

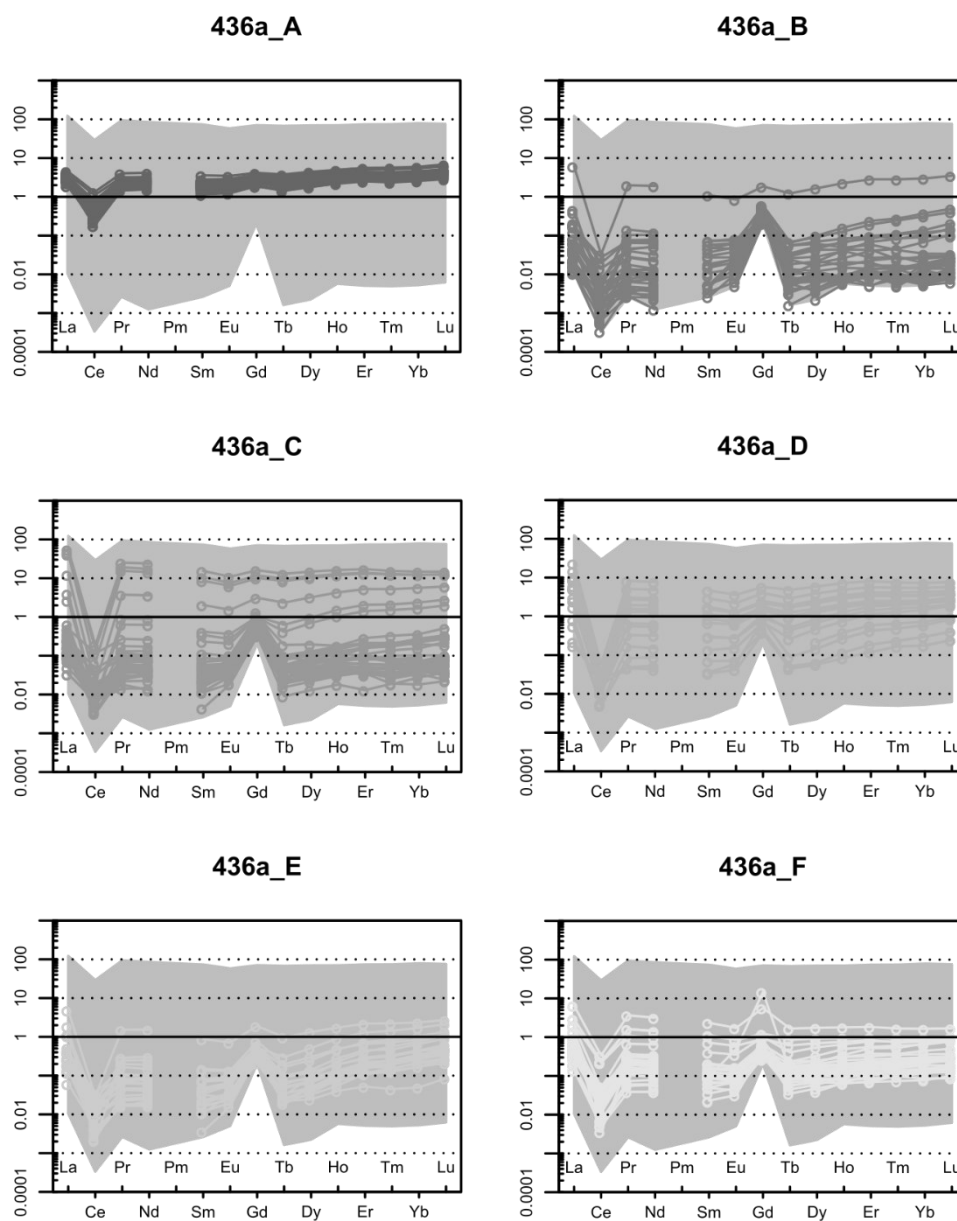


Figure C1. Rare earth element plots of each individual ablation area for sample 17NP436a. Grey shaded area in each diagram represents the range of chondrite normalized REE concentrations in all calcite ablation spots.

17NP436b basalt breccia

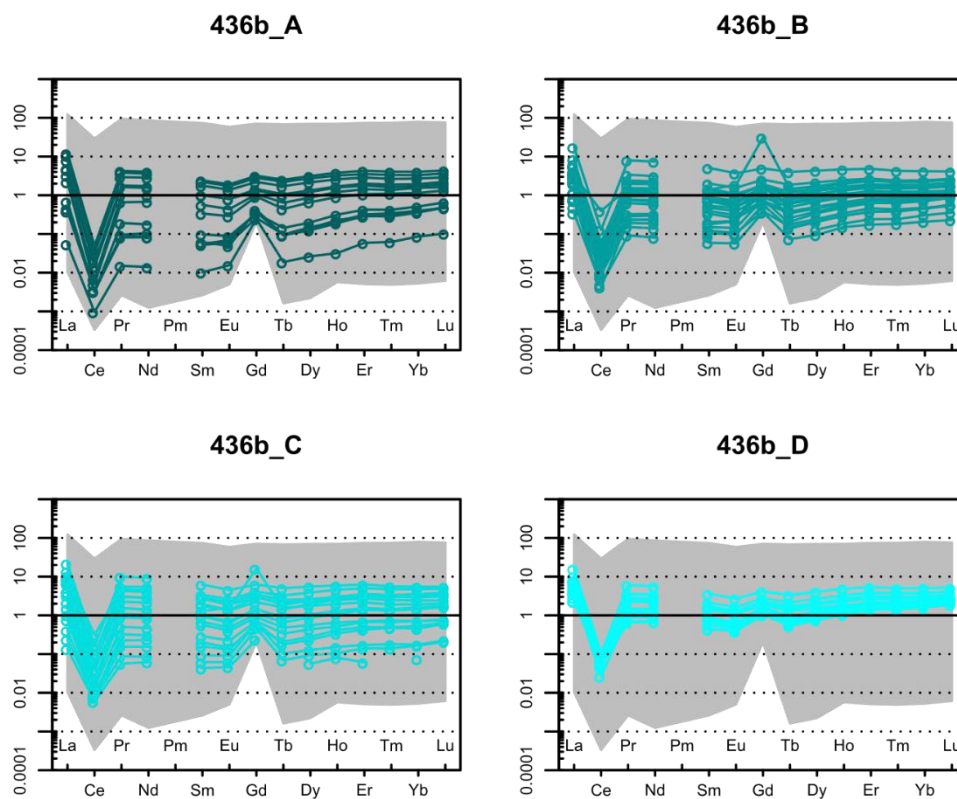


Figure C2. Rare earth element plots of each individual ablation area for sample 17NP436b. Grey shaded area in each diagram represents the range of chondrite normalized REE concentrations in all calcite ablation spots.

15NP233 vesicular basalt

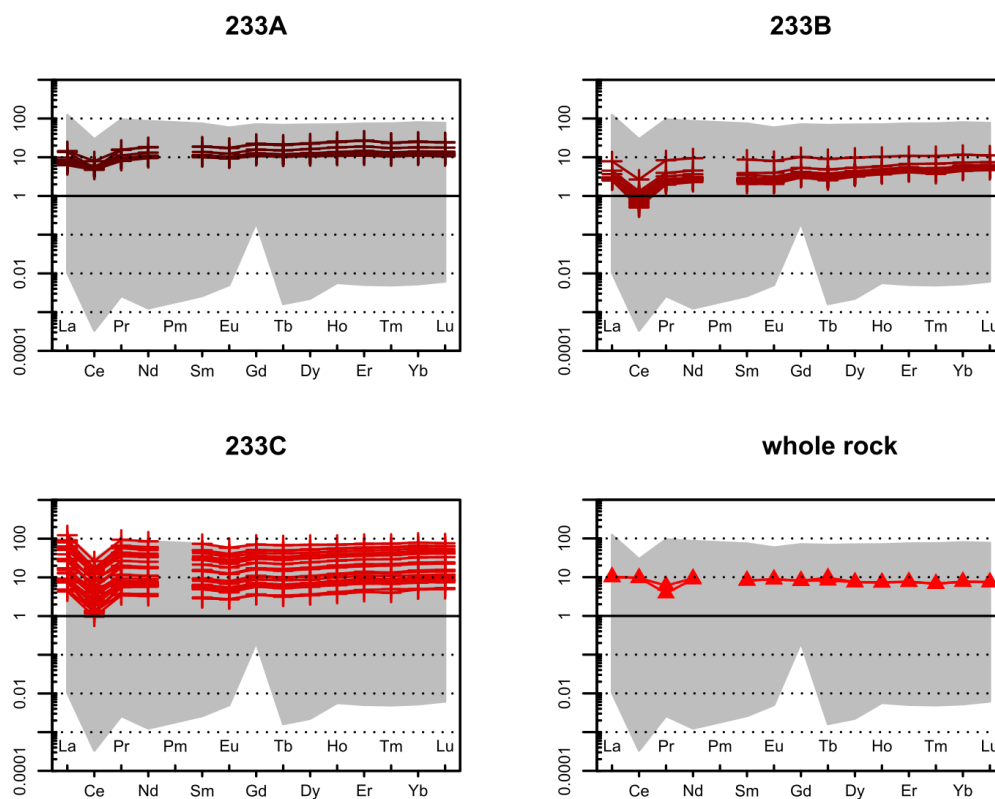


Figure C3. Rare earth element plots of each individual ablation area for sample 15NP233. Whole rock data from Rembe et al. (2021). Grey shaded area in each diagram represents the range of chondrite normalized REE concentrations in all calcite ablation spots.

15NP236 vesicular pillow basalt

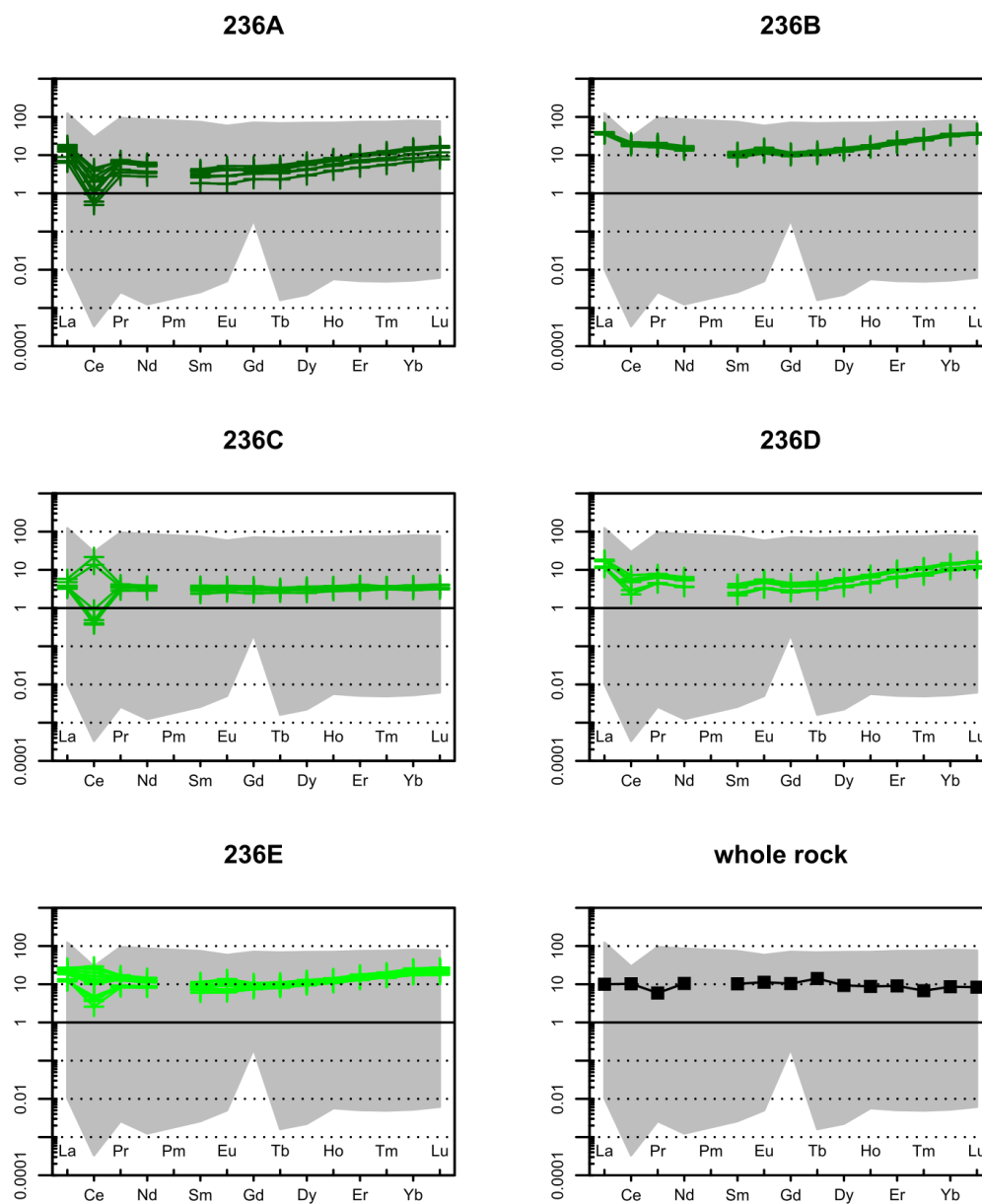


Figure C4. Rare earth element plots of each individual ablation area for sample 15NP236. Whole rock data from Rembe et al. (2021). Grey shaded area in each diagram represents the range of chondrite normalized REE concentrations in all calcite ablation spots.